JGR Oceans

RESEARCH ARTICLE
10.1029/2021JC018213

Key Points:

- Volume transport variability was greatest equatorward of 8°N, at the intersection of North and South Pacific currents
- Subthermocline (lower-layer) interannual volume transport anomalies were of the same magnitude of those of the thermocline (upper-layer)
- Interannual volume transport anomalies in the western tropical North Pacific increased before the mature 2015/2016 El Niño event

Correspondence to:
M. C. Schönau,
mschonau@ucsd.edu

Citation:
Schönau, M. C., Rudnick, D. L., Gopalakrishnan, G., Cornuelle, B. D., & Qiu, B. (2022). Mean, annual, and interannual circulation and volume transport in the western tropical North Pacific from the Western Pacific Ocean State Estimates (WPOSE). *Journal of Geophysical Research: Oceans*, *127*, e2021JC018213. https://doi.org/10.1029/2021JC018213

Received 4 NOV 2021
Accepted 2 MAY 2022

Mean, Annual, and Interannual Circulation and Volume Transport in the Western Tropical North Pacific From the Western Pacific Ocean State Estimates (WPOSE)

Martha C. Schönau[1,2], Daniel L. Rudnick[1], Ganesh Gopalakrishnan[1], Bruce D. Cornuelle[1], and Bo Qiu[3]

[1]Scripps Institution of Oceanography, UC San Diego, La Jolla, CA, USA, [2]Applied Ocean Sciences, Fairfax Station, VA, USA, [3]University of Hawaii at Manoa, Honolulu, HI, USA

Abstract Interannual volume transport anomalies in the far western tropical North Pacific were calculated using the Western Pacific Ocean State Estimates (WPOSE; 2009–2017; 115°E–170°E, 15°S–27°N) to assess the magnitude, phase, and vertical structure of volume transport, and the relationship of interannual transport to the El Niño-Southern Oscillation phenomena. The mean velocity and thermohaline structure for the WPOSE were verified using Argo climatology and autonomous glider observations. Transport was calculated for both an upper layer (surface-26 kg m^{-3}) and a lower layer (26–27.3 kg m^{-3}). Annual volume transport anomalies were small north of 8°N but varied by 50% of the mean volume transport between the equator and 8°N. Interannual anomalies exceeded annual anomalies throughout the region. Volume transports of the North Equatorial Current, the Mindanao Current, and the South Equatorial Current/New Guinea Coastal Undercurrent increased beginning in September 2014, leading to a large increase in transport in the North Equatorial Counter Current before the mature phase of El Niño in 2015/2016. The increase in transport was related to the meridional gradient in thermocline depth centered at 5°N at the southern part of the Mindanao Dome, where extreme shoaling of the thermocline took place. Lower-layer volume transports were not always in phase with those of the upper-layer and made considerable contributions to total transport variability.

Plain Language Summary The Western Pacific Ocean State Estimates (WPOSE) estimate the ocean state by combining observations and ocean model simulations through data assimilation. These estimates were made from 2009 to 2017 in the far western tropical Pacific. This region encompasses warm, tropical surface water and subtropical thermocline water (upper-layer) and polar intermediate water (lower-layer) that are sourced from the North and South Pacific and spread into the Indian Ocean through the Indonesian throughflow. The WPOSE were used to calculate volume transports to understand the modulation of major ocean currents as a system. Annual volume transport variability was small to the north of 8°N, and large to the south of 8°N and near the equator. Interannual volume transport variability was much greater than annual variability for both the upper and lower isopycnal layers and had a clear relationship with the El Niño-Southern Oscillation phenomenon. The period encompassed two El Niño events, a weak event in 2009/2010, and a strong event in 2015/2016. Regional transport increased during both events, but in the 2015/2016 El Niño, an increase in volume transport led the El Niño event by 2–3 months.

1. Introduction

The western tropical Pacific has a warm and relatively fresh pool of water that creates deep atmospheric convection which leads to strong ocean-atmosphere coupling. The distribution of the warm, tropical water across the Indo-Pacific region influences the seasonal monsoons across Asia and interannual temperature and precipitation extremes globally via the interannual El Niño-Southern Oscillation (ENSO) phenomena (Clarke, 2014; Gordon, 1986; Schneider, 1998). The currents in the western tropical Pacific transport these warm, tropical waters, along with subtropical and subpolar water masses (Fine et al., 1994), westward through the Indonesian Throughflow (ITF; Gordon, 1986; Gordon & Fine, 1996), and eastward across the Pacific Basin. Thus, regional volume transport plays a significant role in both annual and interannual climatic variability. However, owing to a lack of synchronous observations, the annual and interannual shifts in volume transport of these currents as a system are not well resolved. Here, we resolve the phase, magnitude, and vertical structure of volume transport

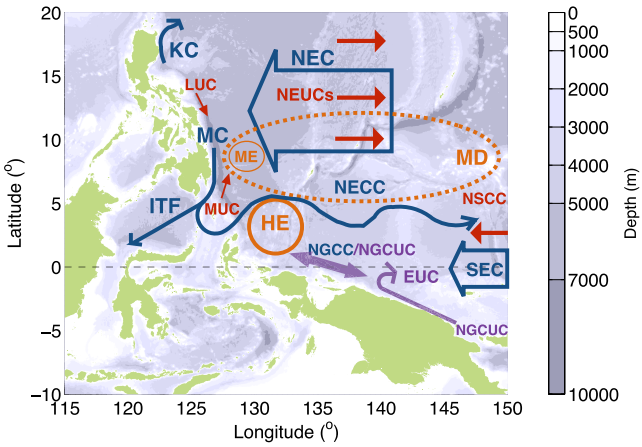

Figure 1. Schematic of the circulation in the tropical northwestern Pacific. Blue is the circulation from the surface to the bottom of the thermocline, typically 200–300 m depth at 26 kg m^{-3}. Main currents are the North Equatorial Current (NEC), the Mindanao Current (MC), the Kuroshio (KC), the Indonesian Throughflow (ITF), and the North Equatorial Counter Current (NECC). At the equator, the South Equatorial Current (SEC) and seasonally reversing New Guinea Coastal Current (NGCC) enter the region. Subthermocline currents (red, >26 kg m^{-3}) flow counter the thermocline circulation. Subthermocline currents are the Luzon Undercurrent (LUC), the Mindanao Undercurrent (MUC), the North Equatorial Currents (NEUCs), and the North Subsurface Counter Current (NSCC). In the South Pacific, the New Guinea Coastal Undercurrent (NGCUC) and the Equatorial Undercurrent (EUC) (purple) span from the lower part of the thermocline into the subthermocline. Cyclonic circulation occurs around the variable Mindanao Eddy (ME), and persistent anticyclonic Halmahera Eddy (HE). In the Spring, the NECC recirculates into the NEC around the Mindanao Dome (MD). The NGCUC surfaces in the North Pacific with the SEC to feed into the NECC around the HE.

through the far tropical western Pacific region using an ocean state estimate to understand how the regional volume transport varies on annual and interannual time scales.

A schematic of the circulation in the far western tropical Pacific is shown in Figure 1. The wind-driven surface to thermocline ocean circulation (Figure 1; blue) was detailed in Klaus Wyrtki's exploration of the region in the 1960s (Wyrtki, 1961) and further determined from ship transects and moorings in later decades (Gouriou & Toole, 1993; Johnson et al., 2002; McPhaden et al., 1998; Toole et al., 1988). In the North Pacific, the North Equatorial Current (NEC) transports subtropical thermocline water and subpolar intermediate water into the region bifurcating near the Philippines into the equatorward Mindanao Current (MC) and poleward Kuroshio Current. The MC, a low-latitude western boundary current, then transports these water masses water along the island of the Mindanao, splitting to feed the ITF and the North Equatorial Counter Current (NECC; Wyrtki, 1961). The NECC, centered near 5°N, flows eastward into the tropical North Pacific. From the south, the NECC is fed by the South Equatorial Current (SEC), the New Guinea Coastal Undercurrent (NGCUC), and the seasonally varying New Guinea Coastal Current (NGCC; Lindstrom et al., 1987; Kuroda, 2000). Beneath the surface and thermocline circulation are notable subthermocline undercurrents that flow opposite to the direction of the upper ocean currents (Figure 1; red); the poleward Mindanao Undercurrent (MUC) beneath the Mindanao Current (MC) (D. X. Hu et al., 1991; Schönau & Rudnick, 2017), the equatorward Luzon Undercurrent (LUC) beneath the KC (Bingham & Lukas, 1994; Qu et al., 1997) and the eastward North Equatorial Undercurrents (NEUCs) beneath the NEC (Qiu et al., 2013; Schönau & Rudnick, 2015). In addition, along the equator, the Equatorial Undercurrent (EUC) flows eastward. These undercurrents have been resolved with moorings, shipboard observations, autonomous floats, and gliders.

The variability of annual and interannual upper ocean transport is attributed to changes in sea surface height (SSH) that are forced by basin-wide and local wind stress. Annual variability in basin-wide wind stress causes Ekman pumping that leads to Sverdrup transport and Rossby waves that propagate westward from the eastern and central Pacific (Kim et al., 2004; Qiu & Lukas, 1996). Local Ekman pumping in the western Pacific occurs in association with the East Asian monsoon (Masumoto & Yamagata, 1991; Tozuka et al., 2002). The interannual SSH variability in the tropical Pacific is dominated by the ENSO dynamics. Satellite absolute dynamic topography (ADT) from Archiving, Validation, and Interpretation of Satellite Oceanographic Data (AVISO), produced and distributed by Copernicus Marine and Environmental Monitoring Service (CMEMS; http://marine.copernicus.eu/) and gridded, monthly Argo climatology (Roemmich & Gilson, 2009) show the footprint and magnitude of annual and interannual variability (Figure 2). Annual anomalies in ADT peak in the eastern and central Pacific near 12°N and 5°N, respectively, and extend in east-west streaks across the basin, indicative of Rossby waves. The annual anomalies are mirrored by changes in thermocline depth (Figure 2c), as calculated from the depth variability of the 23–24 kg m^{-3} isopycnal layer. The interannual anomalies of ADT exceed annual anomalies, peaking along the equator in the eastern Pacific and to the north and south of the equator in the western Pacific (Figure 2b). This pattern is also observed in the thermocline depth (Figure 2d). These coincide with the modes of ENSO. The east-west tilt is the leading mode of thermocline depth variability and is typical of volume transport into and out of the western Pacific (Meinen & McPhaden, 2000). The second mode is asymmetric around the equator and typical of warm water volume (WWV) buildup and discharge at the equator (Meinen & McPhaden, 2000).

The SSH variability impacts circulation, causing geostrophic transport away from the equator and zonal pressure gradients along the equator. During an El Niño, there is on average, an increase in transport in western Pacific currents and a decreased ITF transport, with the opposite occurring during La Niña (D. Hu et al., 2015).

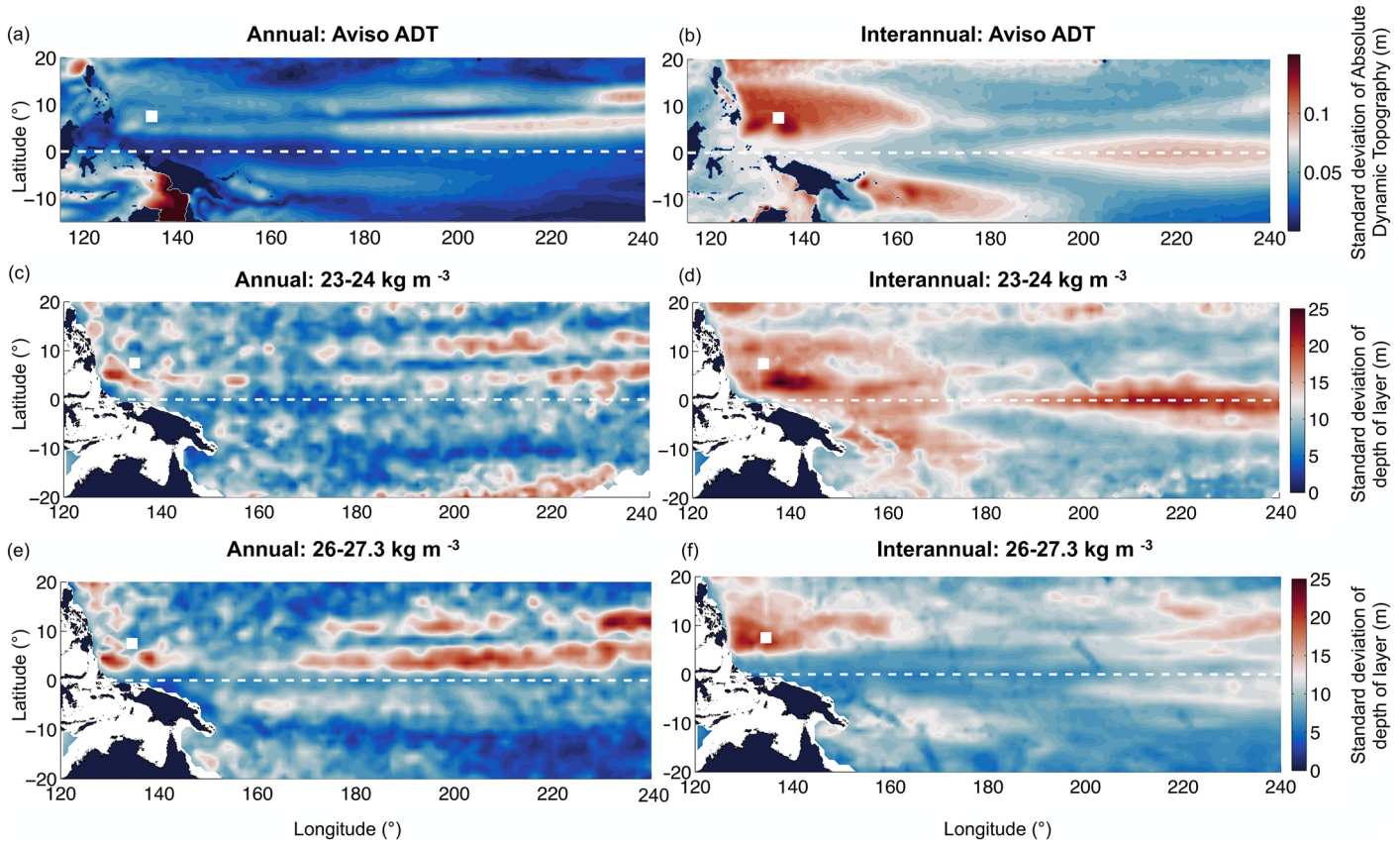

Figure 2. Annual (a, c, e) and interannual (b, d, f) standard deviation of (a, b) absolute dynamic topography (ADT) from AVISO (1993–2015), (c, d) the depth of the 23–24 kg m^{-3} isopycnal layer from Argo climatology, and (e, f) the depth of the 26–27.3 kg m^{-3} isopycnal layer from Argo climatology (ARGO). The depths of the 23–24 kg m^{-3} layer and 26–27.3 kg m^{-3} layer represent an average depth of the thermocline layer and subthermocline layer (defined from base of the thermocline to roughly 1,000 m depth), respectively.

However, these results were based on nonsynchronous hydrographic sections across currents and were not always concurrent with ENSO events. The magnitude and phase of the volume transport as a system are less clear. Studies have found that an increased eastward NECC transport can precede an El Niño, leading to WWV to build in the equatorial region (Hsin & Qiu, 2012b; Johnston & Merrifield, 2000; Meinen & McPhaden, 2001). The increase could be driven by greater transport in the North Pacific (i.e., increases in the NEC/MC), or by greater transport in the South Pacific (i.e., increases in the NGCUC/SEC) circulation.

Below the wind-forced upper-layer, the subthermocline volume transport is often overlooked. However, the transport variability of this layer can be large. For example, in the North Pacific, the variability of the subthermocline transport beneath the MC and NEC exceeded that of the surface to thermocline layer (Schönau & Rudnick, 2015, 2017). There is large annual and interannual variability in the depth of this layer (Figures 2e and 2f), particularly in the MD region, suggesting that transport variability may also be large. However, there is a sparsity in deep historical transport observations, and the dynamics of the subthermocline are not well understood. Some subthermocline dynamics have been attributed to eddies (Chiang & Qu, 2013; Chiang et al., 2015) and Rossby wave interactions (Qiu et al., 2013), but how these translate into transport variability, particularly on annual and interannual timescales is less clear.

This study examines the magnitude and phase of the upper-layer (surface to base of thermocline) and lower-layer (subthermocline to a depth of ~1,000 m) volume transports in the far western tropical Pacific to assess the vertical transport structure, how transport changes as a system, and the relationship of these changes to ENSO. The mean, annual, and interannual transport across discrete transects are derived from a data assimilating Western Pacific Ocean State Estimate (WPOSE), which spans the western North Pacific tropical circulation, the ITF, and inflow from the South Pacific (Figure 3). The transects across the NEC, MC, ITF, NGCUC/SEC, and

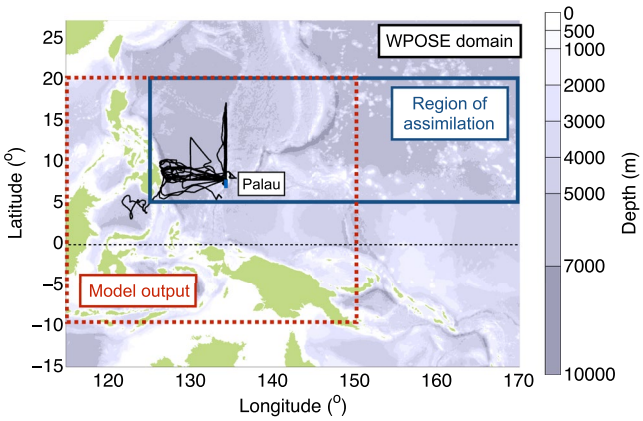

Figure 3. Domain of the Western Pacific Ocean State Estimates (WPOSE). Blue box shows the region of data assimilation. Daily model output is produced at 1/6° horizontal resolution from January 2009 to December 2017, with 50 vertical levels.

NECC bisect the inflow and outflow of the region. The WPOSE period of 2009–2017 encompassed a moderate El Niño in 2009/2010, the "failed" El Niño in 2014 (McPhaden, 2015), and a strong El Niño in 2015/2016 (Santoso et al., 2017). The period was also concurrent with equatorward transport observations in the North Pacific (Schönau & Rudnick, 2015, 2017), South Pacific (Kessler et al., 2019), and the Makassar strait (Gordon et al., 2019), the main channel of the ITF. WPOSE provides a dynamically consistent solution to better understand how the volume transport changes as a system, providing resolution in space and time beyond current observational capabilities. The relationship of local and remote wind-forcing, thermocline shifts, and changes in volume transport to ENSO will be examined. The manuscript is organized as follows: Section 2 describes WPOSE and observational data; Section 3 compares ocean structure and velocity of WPOSE with observations; Section 4 provides annual and interannual volume transports; and Section 5 examines the magnitude and phase of interannual volume transport with respect to ENSO. Section 6 provides a discussion of these results, and Section 7 summarizes the main conclusions.

2. Data

2.1. Western Pacific Ocean State Estimates

Mean, annual, and interannual velocity and volume transports in the western Pacific were calculated from the data assimilative WPOSE through the region bounded by 125°–150°E and 5°S–16.5°N (Figure 3). The WPOSE were produced for the period 1 January 2009, to 31 December 2017, using a regional implementation of the Estimating the Circulation and Climate of the Ocean (ECCO) package (Stammer et al., 2002) for the northwestern tropical Pacific that uses the MIT General Circulation Model (MITgcm; Marshall et al., 1997) and its adjoint-based four-dimensional variational assimilation (4D-Var) system. The WPOSE model domain extended from 115°–170°E, and 15°S–27°N (Figure 3). Temperature and salinity observations from Argo Conductivity Temperature and Depth (CTD) sensors, Expendable Bathythermograph (XBT) and gliders, satellite-derived along-track SSH, and gridded sea surface temperature (SST) covering the region from 122° to 170°E and 5° to 20°N were assimilated into the model. The horizontal resolution of WPOSE is 1/6° and it has 50 vertical z-levels. The vertical level spacing varies by depth, increasing gradually from 2.5 m at the surface to 300 m near the bottom, with a maximum depth of 6,500 m. The model initial conditions and open-ocean boundary conditions for horizontal velocities, temperature, and salinity were interpolated from the data assimilative Hybrid Coordinate Ocean Model (HYCOM/NCODA) 1/12° daily global analysis (Chassignet et al., 2007) and model atmospheric forcing fields were obtained from the NCEP/NCAR reanalysis project (Kalnay et al., 1996). The wind, specific humidity, air temperature, precipitation, and net downward shortwave and longwave radiation were prescribed at the ocean surface.

ECCO uses a four-dimensional variational assimilation (4D-Var) method (Heimbach et al., 2002) that adjusts model control variables to create a model simulation that minimizes the misfit between the model solution and real observations at the places and times of the observations. The model controls are temperature and salinity initial conditions, open-ocean boundary conditions, and atmospheric forcing fields. Each state estimate is a free-running dynamically consistent solution forced using adjusted model controls and conserves heat, salt, mass, and momentum. The WPOSE solution for the period 2009–2017 was created by combining 27 sequential, non-overlapping 4-month estimates. Each 4-month-long state estimate was initialized using HYCOM/NCODA solutions (reference state or "first guess" solution). The 4DVAR data assimilation is an adjustment of the data assimilative HYCOM/NCODA solution for a 4-month period before it is reinitialized from HYCOM/NCODA. To evaluate the benefits of data assimilation, SSH from WPOSE and HYCOM/NCODA were compared with AVISO gridded SSH (not shown). The Root-Mean-Square-Difference (RMSD), averaged over the data assimilation region and the 27 state estimates was 0.05 m for the first 30 days, similar to that of HYCOM/NCODA, and slowly increased to 0.07 m after 120 days. It should be noted that WPOSE matches data over a 4-month model run, whereas HYCOM/NCODA solutions are updated daily. Comparisons of data assimilative hindcasts and forecasts with dependent and independent observations, and discussions on the importance of data assimilation using

a similar MITgcm-ECCO 4D-Var system can be found in Gopalakrishnan et al. (2013). WPOSE solutions have previously been compared to glider observations (GOs) and the Parallel Ocean Program (POP) model (McClean et al., 2011) across the NEC (Qiu et al., 2015), and the MC (Schönau et al., 2015), to independent observations of the mean velocity across the Kuroshio from moorings near the Luzon Strait (Lien et al., 2015), and to independent temperature observations at the western Pacific islands of Palau and Pohnpei (Schramek et al., 2019). The WPOSE were archived as daily averaged fields for temperature, salinity, and absolute horizontal and vertical velocities. The daily output was averaged by month to compare to ARGO and to extract annual and interannual transport anomalies.

2.2. Observations

Autonomous underwater glider observations (GO; 2009–2014; Schönau & Rudnick, 2015) and Argo climatology (ARGO; 2004–2018; Roemmich and Gilson, 2009) were used to verify WPOSE stratification and absolute velocity. Temperature and salinity profiles from GO and Argo were assimilated into WPOSE and the comparison of these observations with WPOSE is perforemd in the following section to assess how well the state estimate hindcast matches the observations. Autonomous underwater Spray gliders, equipped with a Sea-Bird CTD and Seapoint fluorometer, were deployed from Palau at 7.5° and 134.3°E from June 2009 to January 2014. These gliders made 19 transects across the NEC (Schönau & Rudnick, 2015) and 16 transects across the MC (Schönau & Rudnick, 2017; Figure 3) at all times of the year and during one full ENSO cycle. There were a slightly greater number of transects of the NEC from June to November, and of the MC from September to February; however, overall seasonal bias was low. The gliders profiled in a horizontal saw-tooth pattern from the surface to a depth of 1,000 m and recorded observations during each ascent. Observations were binned vertically by 10 m and had a horizontal resolution of roughly 6 km. Depth-averaged velocity was obtained from dead-reckoning (Davis et al., 2008; Todd et al., 2011) and used as a reference velocity for geostrophic velocity. For the comparison of mean velocity structure across the NEC, all glider observations were objectively mapped together along 134.3°E using a Gaussian autocovariance with a length scale of 80 km (Schönau & Rudnick, 2015).

Monthly and mean Argo climatology (ARGO; Roemmich & Gilson, 2009) are produced by mapping Argo float observations in space and time. Argo floats are equipped with CTDs and maintain a drift depth of 1,000 m for 9 days and then profile from a depth of 2,000 m to the surface. There were roughly 35,000 profiles from 300 floats in the WPOSE domain from January 2004 to December 2017, the period over which we examine the WPOSE. The mean climatology for temperature and salinity are available at 1/6° resolution, annual cycle at 1/2°, and monthly anomalies at 1° (https://sio-argo.ucsd.edu/RG_Climatology.html). Geostrophic velocities were calculated from the climatology using the thermal wind equation, referenced to a level of no-motion at 2,000 m, which provides an accurate transport in the subtropical gyre (Schönau & Rudnick, 2015), but may underestimate the transport nearer to topography (Schönau et al., 2015). ARGO provides estimates of velocity and transport across the NEC, and part of the NECC to compare to WPOSE, as well as good spatial coverage of steric height and thermocline depth.

3. Comparison of WPOSE to ARGO and GO

Using 4D-Var data assimilation, WPOSE provides a dynamically consistent solution while trying to create a best-fit to assimilated observations. Although ARGO and GO are not independent observations, they provide the best observational estimates of the mean velocity and stratification. It is of interest to see how the mean thermohaline structure, velocity, transports, and time-varying sea-surface height compare between WPOSE and observations, as even with sophisticated models can contain biases. Moreover, WPOSE 4D-Var 4-month state estimates do not guarantee an exact match to the observations, and this model-data comparison verifies that the 4D-Var assimilation system performs as expected, moving the model trajectory close to the observations.

3.1. Velocity, Transport, and Thermohaline Structure

The mean velocity, transports, and thermohaline structure are compared between WPOSE, ARGO (from 1/6°, mean fields), and GO along a longitudinal transect at 134.3°E, spanning the NEC, NECC, and SEC/NGCUC from 1°S to 16.5°N (Figure 4a). The transect aligns with glider observations of the NEC from Palau at 8°N–16.5°N (Figure 4b). Although the observations and WPOSE are averaged over different periods (ARGO: 2004–2017,

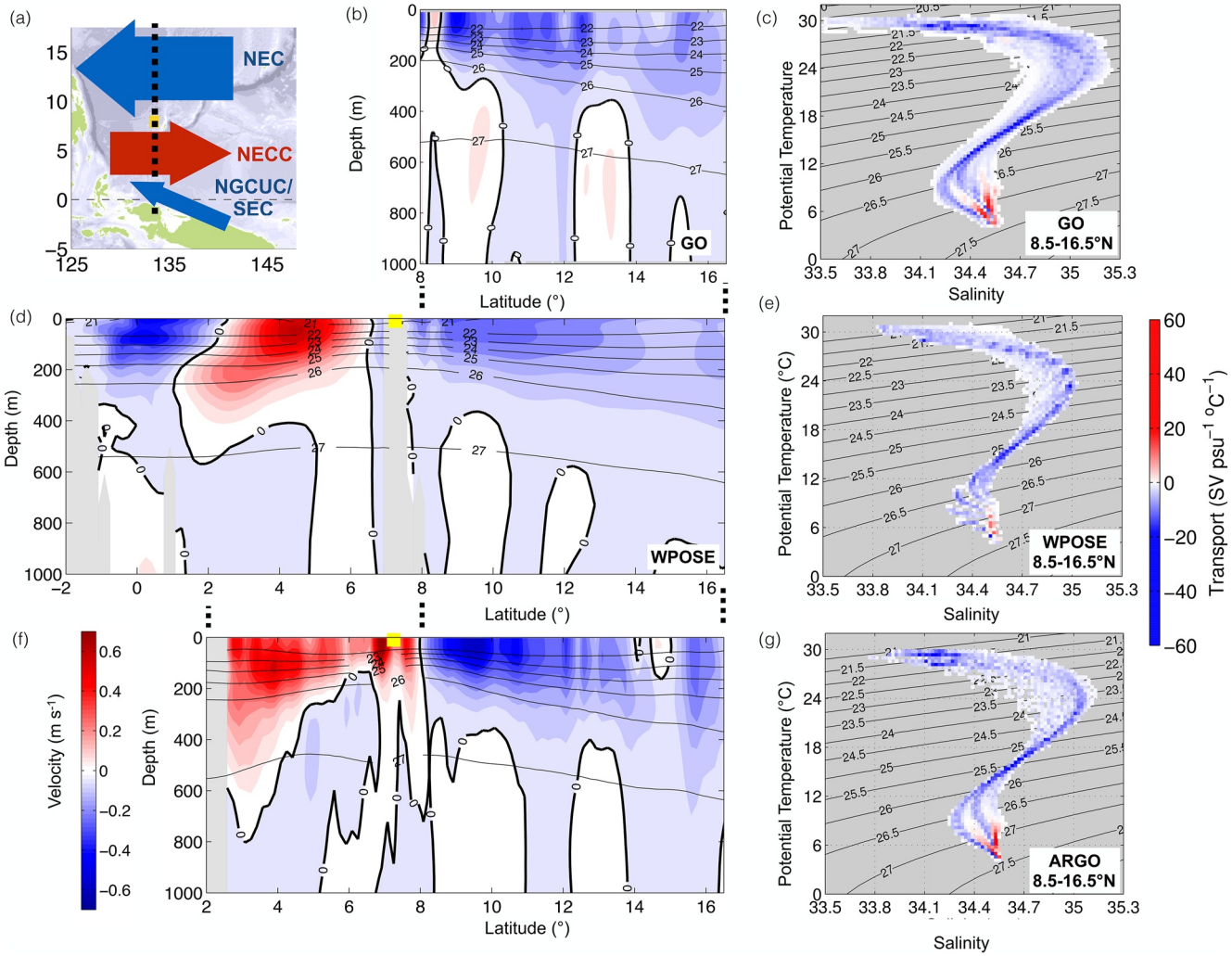

Figure 4. Comparison of velocity and thermohaline transport at 134.3°E. (a) Schematic of transport at 134.3°E. Mean zonal velocity and potential temperature-salinity (TS) binned transport from (b, c) Glider Observations (GO), (d, e) WPOSE, and (f, g) ARGO. Velocity scale is provided in panel (f). For the TS transport diagrams (panels c, e, g) ARGO and WPOSE transports were binned by 0.02 psu and 0.4°C for each month in the annual cycle, summed, and divided by the bin size and the number of months (12). For GO, transport was binned by 0.02 psu and 0.4°C for each objectively mapped transect across the NEC and divided by the bin size and number of transects (19). Positive (red) is eastward velocity or transport. Negative (blue) is westward velocity or transport.

GO: 2009–2014, and WPOSE: 2009–2017), their spans overlap, and are likely lengthy enough that a reasonable comparison can be made.

North of 8°N, GO (Figure 4b) and ARGO (Figure 4f) show a mean westward NEC that is strongest between 8° and 13.5°N from the base of the thermocline (26 kg m^{-3}) to the surface. Two subthermocline undercurrents, centered at 9.6° and 13.1°N, respectively, flow eastward deeper than 26 kg m^{-3}. WPOSE has similar velocity structure but with slightly weaker velocities (Figure 4d), and the core of the second subthermocline undercurrent is slightly shifted to the south (12°N). To the south of Palau, between 2.5° and 7.5°N, both WPOSE and ARGO show a strong eastward NECC, extending as deep as 27 kg m^{-3}. Geostrophic velocity calculations were not made within ±2.5° of the equator for ARGO, but WPOSE captures the westward inflow of the NGCUC/SEC from the island of New Guinea to 2°N. At this longitude, the NGCUC/SEC currents of WPOSE are in a combined state and are indistinguishable. A similar transect along 145°E of the WPOSE shows NGCUC as a subsurface westward current close to the island of New Guinea, and surface westward flow from the SEC at the equator (Schönau, 2017).

Integrating across the NEC (8°–16.5°N), the total mean volume transport for WPOSE (−37.9 Sv) compares favorably to observational estimates from GO (−37.6 Sv) and ARGO (−35.0 Sv). Volume transports for each of the upper

Table 1
Mean Volume Transports and Standard Deviations Across the NEC, NECC, MC, and SEC/NGCUC/EUC for Each Gliders (GO), Argo Climatology (ARGO), and WPOSE (the Western Pacific Ocean State Estimates)

NEC 134.3°E, 8°–16.5°N	Total	Surface – 26 kg m^{-3}	26–27.3 kg m^{-3}	Annual standard deviation	Interannual standard deviation
GO	−37.6	−33.1	−4.5	–	–
ARGO	−35.0	−27.4	−7.5	4.2	5.1
WPOSE	−37.9	−30.9	−7.0	4.3	10.0
NECC 134.3°E, 2.5°–8°N		Surface – 26 kg m^{-3}	26–27.3 kg m^{-3}	Annual standard deviation	Interannual standard deviation
ARGO	35.0	28.4	6.6	8.5	11.6
WPOSE	31.0	26.5	4.4	8.9	16.9
MC 8.5°N, 126.6°–130°E		Surface – 26 kg m^{-3}	26–27.3 kg m^{-3}	Annual standard deviation	Interannual standard deviation
GO	−25.6	−21	−5.1	–	–
ARGO	−7.7	−6.0	−1.7	–	–
WPOSE	−29.5	−20.4	−9.0	3.7	7.6
NGCUC/NGCC/SEC 134.4°E, −2°S to 2°N		Surface – 26 kg m^{-3}	26–27.3 kg m^{-3}	Annual standard deviation	Interannual standard deviation
WPOSE	−12.9	−13.7	0.9	8.6	14.0

Note. Standard deviations are for total annual transport, and the total interannual transport with the annual cycle removed.

(surface to 26 kg m^{-3}) and lower (26–27.3 kg m^{-3}) layers are similar (Table 1). Table 1 also provides mean transports across the NECC, from 2.5° to 8.0°N, and across the MC. For the NECC, ARGO and WPOSE mean transports are comparable within a difference of 4 Sv. At 145°, as a comparison where no data assimilation occurs, the transports from 2° to 5°N between ARGO and WPOSE are in statistical agreement. For the MC, WPOSE and GO transports are similar, within a difference of 3.9 Sv. It should be noted that for the MC, ARGO has an erroneous transport as it does not capture the depth penetration of the equatorward subthermocline MC near the coast (Schönau et al., 2015).

The thermohaline characteristics of volume transport impact the heat transport in and out of the western Pacific. However, models often have biases in subsurface temperature and salinity. A comparison of WPOSE to ARGO and GO water mass transport shows that the volume transport is accurately distributed by temperature and salinity. The volume transport is plotted as a function of thermohaline structure in a composite temperature-salinity (TS) diagram by binning volume transport by temperature and salinity along 134.3°E from 8.0°N to 16.5°N (Figures 4c, 4e, and 4g). For each objectively mapped GO transect, the volume transport for each grid cell was binned by temperature and salinity, then normalized by the bin size (yielding units of Sv $psu^{-1}{}^{\circ}C^{-1}$). The bin size for temperature was 0.4°C and for salinity was 0.02 psu. The volume transport in each bin was then summed over the transects and then divided by the total number of transects (19). For WPOSE (Figure 4e) and ARGO (Figure 4g), the "transects" correspond to the volume transport for each month of the annual cycle. Following the GO transport analysis, the volume transport of WPOSE and ARGO of each grid cell was binned by the temperature and salinity, summed over all months, and divided by the number of months (12) and bin size (0.4°C and 0.02 psu; Figures 4e and 4g). Each TS diagram for WPOSE, ARGO and GO thus shows the expected thermohaline transport of the NEC over a typical year and integrates over temperature and salinity to the respective mean transport of the NEC. Greater variance in temperature and salinity was expected and observed in the TS transport diagram for GO, as it was made from synoptic transects and not monthly averages, as those from WPOSE and ARGO. Additional composite TS transport diagrams along 145°E and 8.5°N can be found in Schönau (2017).

TS transport diagrams from observations and WPOSE show the westward transport of the North Pacific Tropical Water (NPTW; 23.5 kg m^{-3}), identified by its subsurface salinity maximum (Fine et al., 1994; Tsuchiya, 1968).

Below the thermocline, there is a subsurface salinity minimum indicative of North Pacific Intermediate Water (NPIW; 26.5 kg m^{-3}; Fine et al., 1994; Talley, 1993). The temperature and salinity characteristics of the subthermocline undercurrents are visible as eastward transport at densities greater than 26 kg m^{-3}. GO and ARGO have two distinct undercurrents, with the saltier core corresponding to the lower latitude undercurrent (Figures 4c and 4g). WPOSE has an eastward undercurrent transport with one salinity core (Figure 4e). Thus, although the undercurrent velocities are weak in the mean transect (Figure 4d), the TS transport diagram shows that WPOSE has significant undercurrent transport. This implies that the lower-layer transport for ARGO and WPOSE, −7.5 and −7.0 Sv, respectively, may have similar eastward and westward components.

3.2. Isopycnal Depth Variability

The equatorial region (2°S to 2°N) has strong, variable zonal currents and cross-equatorial flow. WPOSE did not assimilate observations south of 5°N, therefore a comparison of WPOSE in this region to observations builds greater confidence in the solution for the regions outside the assimilation domain. As geostrophic transport depends on the meridional gradients of isopycnals, one method is to compare the mean depths of isopycnal layers and perform cross-correlation in the isopycnal depth variability between WPOSE and ARGO. Isopycnal depth is relevant not only to transport but also to the heat content of the equatorial region (e.g., Rudnick et al., 2021).

The depth-averages of isopycnal layers are shown in Figure 5 for both ARGO and WPOSE for each a thermocline (23–24.5 kg m^{-3}) and a subthermocline (26–27.3 kg m^{-3}) layer. In the thermocline, shoaling between 5° and 10°N stretches eastward from the island of Mindanao at 126.6°E. This is indicative of the Mindanao Dome (MD), caused by Ekman suction associated with the East Asian Monsoon (Masumoto & Yamagata, 1991). For ARGO, the shoaling extends to 140°E (Figure 5a), whereas for WPOSE the shoaling extends to 134°E (Figure 5b). There is also a depth discrepancy between ARGO and WPOSE south of 5°N, from 130° to 135°E, that disappears gradually moving eastward and southward. In the subthermocline (26–27.3 kg m^{-3}; Figures 5c and 5d), WPOSE and ARGO have a similar depth structure, with WPOSE shoaling near topographic features that are unresolved by ARGO. ARGO also has a shallower isopycnal layer to the south of 5°N.

Taking a monthly time series of these depth-average isopycnal layers and calculating the correlation coefficient between WPOSE and ARGO provides a measure of the agreement of their low-frequency variability (Figures 5e and 5f). In the thermocline there was good agreement, with correlations exceeding 0.8 throughout most of the region (Figure 5e). The correlation was the lowest (∼0.5) centered at 5°N, 133°E, near the location of the Halmahera Eddy. This is unsurprising, given the strong currents and barotropic instability in the region (L. Chen et al., 2014; X. Chen et al., 2015). Similar cross-correlation analysis using the entire upper layer (surface-26 kg m^{-3}) yields similar results (not shown). In the subthermocline, the correlation between ARGO and WPOSE was greater than 0.8 north of 5°N, and lower to the south (Figure 5f). The subthermocline currents are relatively strong and highly very variable to the south of 5°N (Figures 6 and 7), with evidence of subthermocline eddies (Azminuddin et al., 2021).

Overall, WPOSE has good agreement with observations, providing reasonable estimates of mean velocity, transport, thermohaline characteristics, and depth structure. The greatest discrepancies with observations appeared in the subthermocline and will be further discussed in Section 6.

4. WPOSE Velocity

4.1. Annual Cycle

The WPOSE annual velocity and mean isopycnal depth for the upper (surface-26 kg m^{-3}) and lower (26–27.3 kg m^{-3}) layers are shown in Figure 6. The upper layer encompasses the surface flow to the base of the thermocline, while the lower layer flow extends from the base of the thermocline to an isopycnal that is at about 1,000 m depth. The base of the thermocline was chosen at 26 kg m^{-3} as a reasonable separation between upper and lower layers, as it separates the thermocline and subthermocline transport in the NEC (Schönau & Rudnick, 2015), the MC (Schönau & Rudnick, 2017), and the NECC (Hsin & Qiu, 2012b; Johnson et al., 2002). Figure 4 provides additional evidence, with the mean velocity of the NGCUC/NGCC/SEC, NECC, and NEC above the 26 kg m^{-3} isopycnal. The lower limit of the subthermocline layer was chosen at 27.3 kg m^{-3}, which is the deepest isopycnal surface that was consistently shallower than 1,000 m across the domain (Schönau & Rudnick, 2015, 2017).

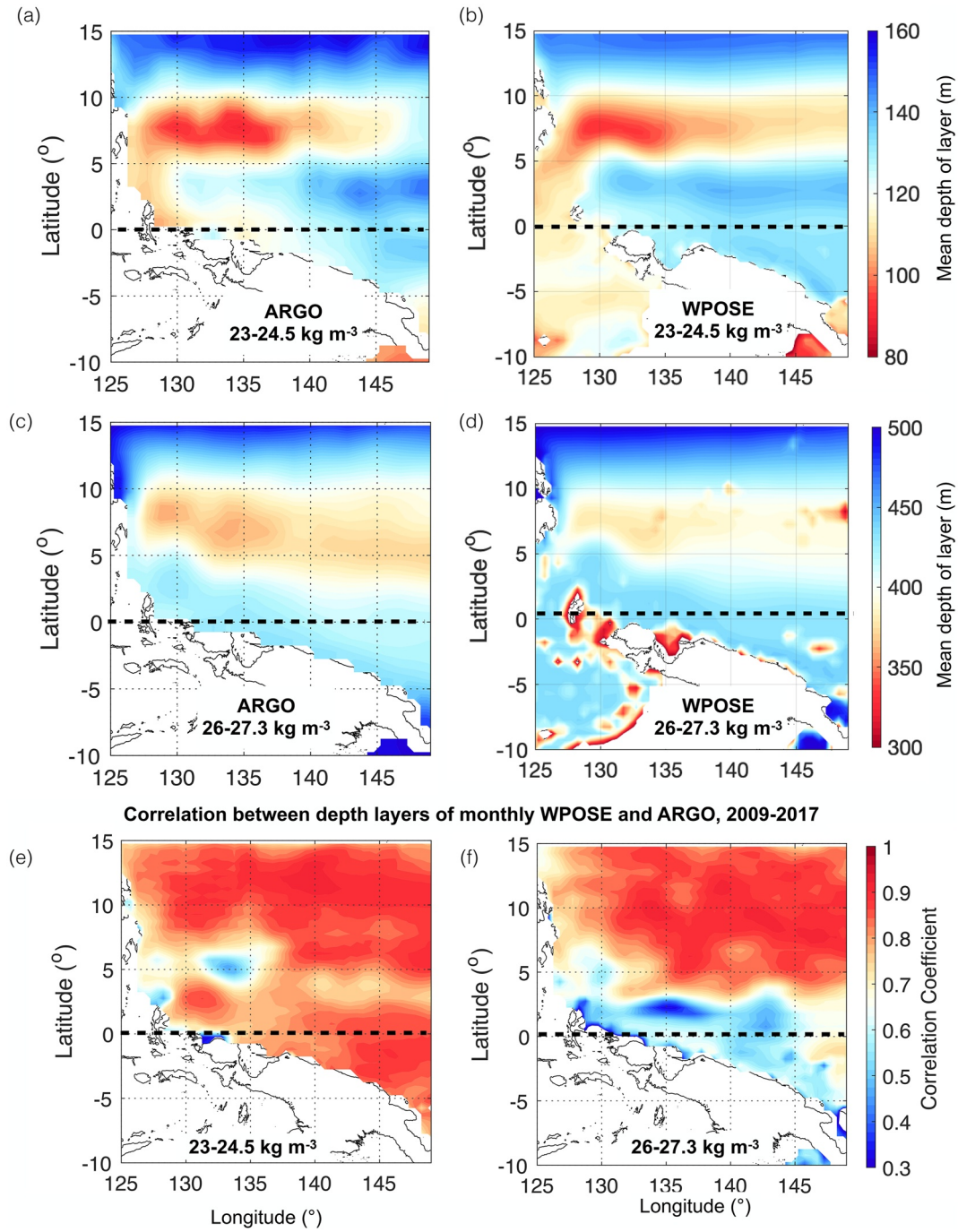

Figure 5. Comparison of depth structure between WPOSE and ARGO. Mean depth of the 23–24.5 kg m^{-3} layer for (a) ARGO and (b) WPOSE. Mean depth of the 26–27.3 kg m m^{-3} isopycnal layer for (c) ARGO and (d) WPOSE. Correlation coefficient between monthly averaged ARGO and WPOSE for the mean depths of the (e) 23–24.5 and (f) 26–27.3 kg m m^{-3} isopycnal layers.

The velocities in the upper and lower layers have significant annual variability. Away from the equator, the mean flow is geostrophic, perpendicular to the gradient in depth for each layer (i.e., velocities are along the lines of constant depth). Several currents are identifiable. In the upper layer (Figures 6a–6d), the westward NEC flows north of 8°N, impinging on the Philippines and bifurcating between 13° and 14°N. The highest latitude bifurcation occurs between October and January, consistent with previous observational and theoretical estimates (Qiu

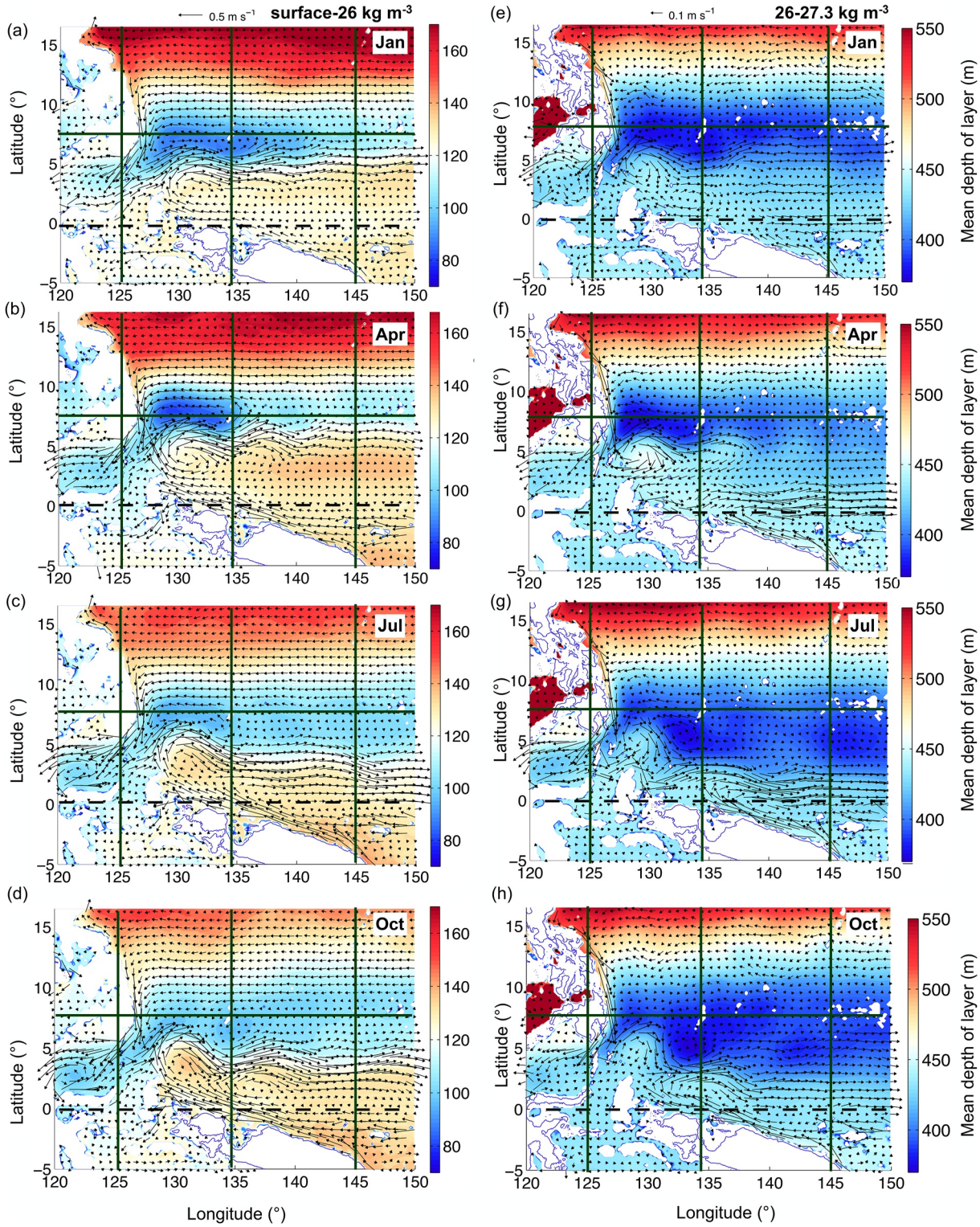

Figure 6. Annual velocity and depth averaged over (a–d) the upper (surface-26 kg m^{-3}) and (e–h) the lower (26–27.3 kg m^{-3}) layers for (a, e) January, (b, f) April, (c, g) July, and (d, h) October. The vector scale is 0.5 m s^{-1} for the left panels and 0.1 m s^{-1} for the right panels, shown at top. Solid lines at 125°E, 134.3°E, 145°E, and 8°N are shown to help assess differences between the panels and are a few of the bounds used to assess transport variability in Section 5.

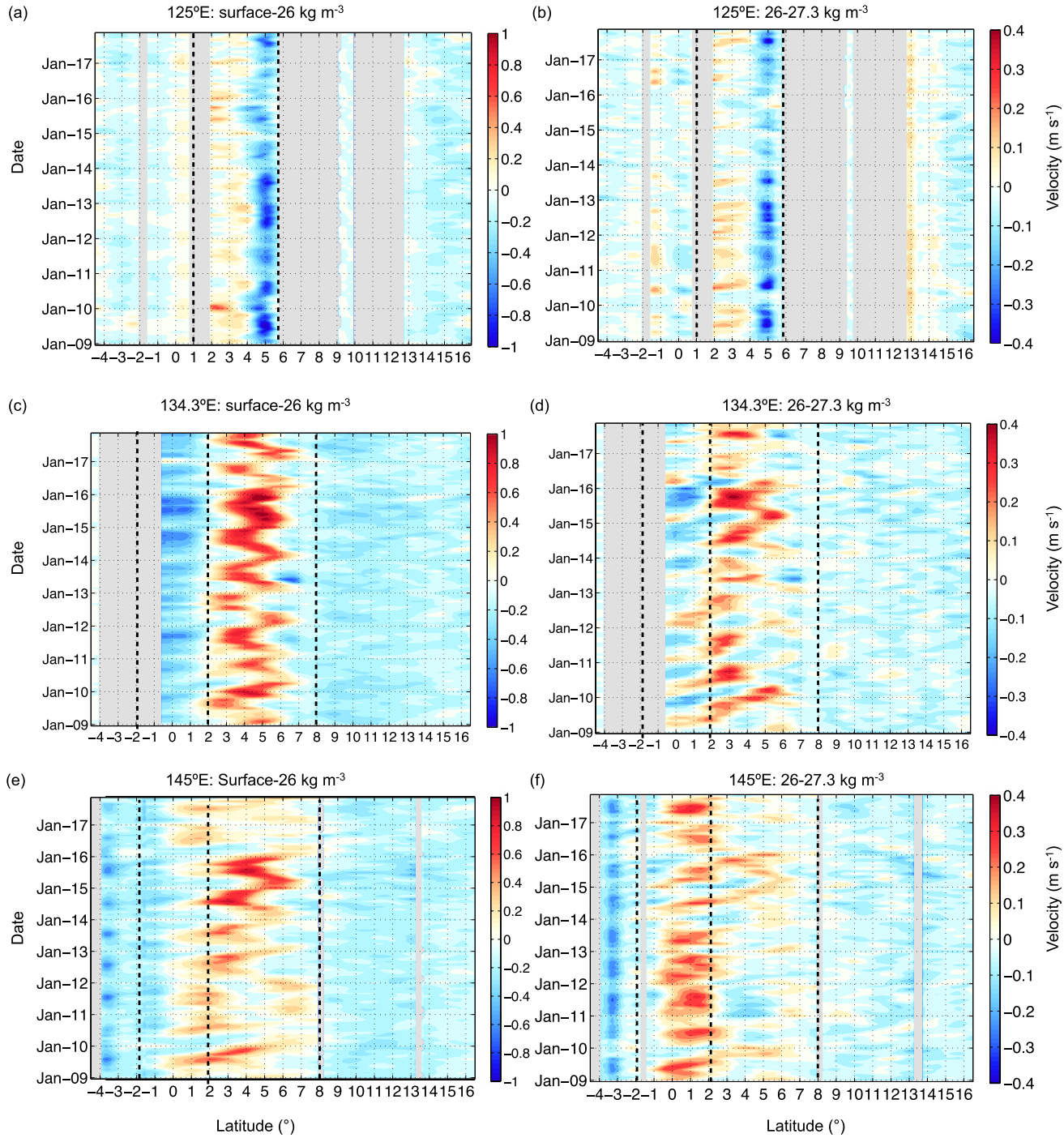

Figure 7. WPOSE monthly zonal velocity averaged over (a, c, e) upper (surface-26 kg m^{-3}) and (b, d, f) lower (26–27.3 kg m^{-3}) layers along (a, b) 125°E, (c, d) 134.3°E and (e, f) 145°E. Dashed lines show transport boundaries for annual and interannual transport calculations.

& Lukas, 1996; Qu & Lukas, 2003). The MC flows equatorward along the coast of the Philippines, splitting at roughly 5°N into the westward ITF and eastward NECC. The location of this split and the amount of retroflection of the ITF flowing back to the NECC varies month to month. Currents are strong in the region from 125° to 134.3°E, and from the equator to 8°N, where the HE is located. Centered around 131° and 4°N, the HE is fed from the west by the MC and south from the NGCUC/NGCC/SEC, serving as the initiation point of the NECC.

The NECC is the strongest current in the region, exceeding 1 m s^{-1}, and varies in both strength and location. After its strong start in the HE, the NECC is northernmost in winter (Figure 6a), and southernmost in summer (Figure 6c), consistent with observations (Hsin & Qiu, 2012a). The latitude of the NECC appears to be related to the build-up of the MD (Kashino et al., 2011), centered at 8°N between 127°E and 144°E (Figures 6a and 6b), that occurs in late winter and early Spring from northeasterlies that create Ekman suction. This causes part of the NECC to recirculate northward, flowing back into the NEC. By July, the MD has been dissipated by the arrival of Rossby waves and changes in regional wind-stress (Tozuka et al., 2002). The strength of the NECC varies throughout the year, with the greatest eastward velocities occurring late in the second half of the year, when the NECC is at its southernmost point and northward recirculation to the NEC does not occur. The velocities and extent of the inflow from the NGCUC/NGCC/SEC are also strongest in the second half of the year, and weakest in January. This is consistent with synoptic observations of the reversal of the NGCC, which flows southward along the surface in January, and strengthens the equatorward NGCUC in summer (Kuroda, 2000; Ueki, 2003). Here, both the NGCUC and NGCC are averaged together in the upper layer.

In the lower layer, velocities are typically one-fifth to one-third of those in the upper layer, as noted in the velocity scale (Figures 6e–6h). North of 8°N, the circulation is weak, and generally flows in the same direction as the surface flow. It is difficult to discern the NEC undercurrents, but they could be small with respect to the chosen scale. South of 8°N, the velocity direction in the lower layer is more variable than that of the upper layer. In January, the currents are weak and the subthermocline component of the NECC is at its northernmost extent beneath the upper layer of the NECC. This deep component of the NECC is consistent with the North Subsurface Counter Current (NSCC; Gouriou & Toole, 1993). There is very little inflow from the South Pacific during this time, with the lower part of the NGCUC feeding directly into the eastward equatorial flow of the EUC (Tsuchiya et al., 1989). There is also a subsurface westward jet centered at 3°N below the NECC. By the middle to the end of the year, the subthermocline HE and NECC flow strengthen, combine with inflow from the NGCUC, and flow eastward to the EUC. However, it is not necessarily in phase or along the same latitude as the upper-layer NECC. By October, the eastward flow begins a northward trek, continuing to receive inflow from the NGCUC. The EUC moves slightly northward of the equator from 140° to 150°E. The large variability and linkages between the NGCUC/EUC and NECC/NSCC are consistent with previous observations and model output (Dutrieux, 2009; Gouriou & Toole, 1993; Kawabe et al., 2008).

4.2. Variability: 125°, 134.3°, and 145°E

From the annual cycle (Figure 6), it is evident that there are strong zonal velocities into and out of the region (5°S–16.5°N; 125°–145°E). To assess the velocity variability, and determine transport bounds, latitudinal transects of velocity averaged over the upper and lower layers were made at 125°, 134.3°, and 145°E (Figure 7). These transects encompass the ITF (125°E; Figures 7a and 7b), the NGCUC/NGCC/SEC (134.3°E; Figures 7c and 7d), and NEC (145°E; Figures 7e and 7f). The ITF had strong westward flow in the upper layer, and substantial velocity in the lower layer between 4° and 6°N. A return eastward current from the Sulawesi Sea existed between 2° and 4°N. The annual cycle (not shown) had the strongest velocities between May and October, consistent with observations in the Makassar Strait (Gordon et al., 2019). There was notable interannual variability in the ITF, with strong velocities before January 2014 and after January 2017, and relatively weak velocities during the 2015/16 El Niño. These are consistent with the notion of a reduced ITF during El Niño (D. Hu et al., 2015). However, the eastward return velocity was not necessarily in phase with the westward flow, nor was there a correspondence in the velocities between the upper and lower layers.

At 134.3°E (Figures 7c and 7d), there was westward flow north of 7°N from the NEC, and south of 2°N from the NGCUC/NGCC/SEC. The eastward NECC between 2°N and 7°N, had an annual north-south meander, and an interannual intensification from January 2014 to January 2016, preceding and during the 2015/2016 El Niño. Velocities were weaker but more variable in the lower layer, particularly beneath the NECC and NGCUC/NGCC/SEC (Figure 7d). Some eastward velocities occurred beneath the NEC, which could be weak evidence of the undercurrents, but the flow was primarily westward.

At 145°E (Figures 7e and 7f), the eastward NECC was significantly wider in the upper layer, extending from the equator to 8°N with notable annual variability. There was a small increase in velocity in 2009 (3°–5°N) and a substantial velocity increase in 2014/2015. In the lower layer, eastward velocities were strong and organized along the equator, as the NGCUC outflow and subthermocline NECC/NSCC merged into the EUC.

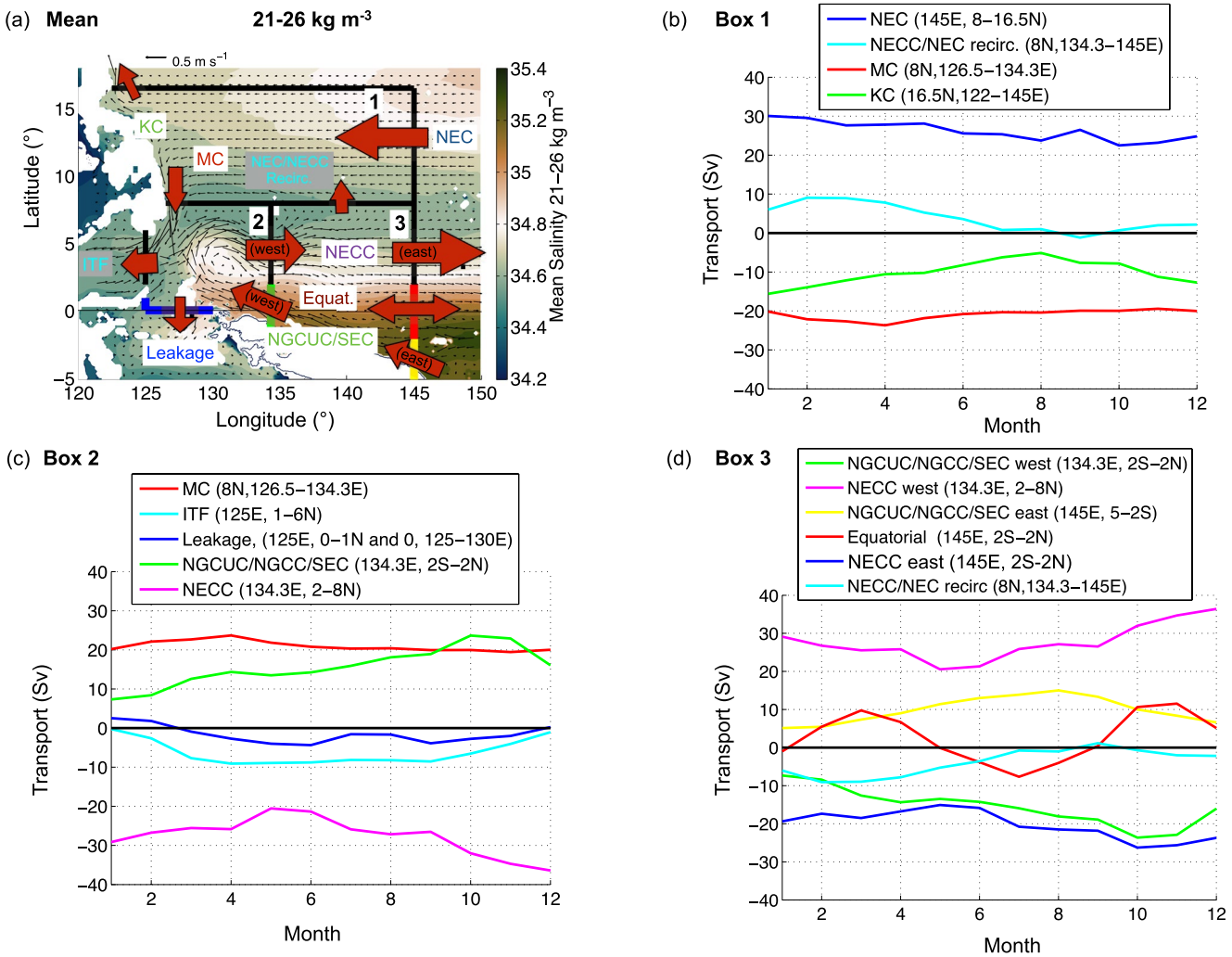

Figure 8. (a) WPOSE mean velocity (arrows) and salinity (color contours) in the upper layer (surface-26 kg m^{-3}). Boxes (Boxes 1–3) indicate the partitions for annual transport. Arrows label main currents. Upper-layer annual volume transport for (b) Box 1, (c) Box 2, and (d) Box 3. Transport into the box is positive and transport out of the box is negative. Green (yellow) lines along 134.3°E (145°E) indicate the bounds for the NGCUC/SEC west (east) transport. The red line at 145° indicates the bounds of the equatorial transport. Mean transport, and annual and interannual standard deviations of transport are given in Figure 10.

5. Regional Transport

Transport bounds were chosen to reflect the major circulation pathways and annual and interannual velocity variability in each of the upper and lower layers. North of 8°N, velocities are steady with little variability. Transport bounds along 8° and 16.5°N encompass the NEC transport and at its bifurcation, the equatorward transport of the MC, and the poleward transport of the KC (Figures 7c–7f). South of 8°N, the velocity variability in both the upper-layer and lower-layer is large making it difficult to set transport bounds. To separate the mean eastward outflow of the NECC from the westward inflow of the NGCUC, and to be cognizant of the different dynamics in the equatorial region, transport bounds were set at topography in the southern hemisphere, 2°S, 2°N, and 8°N (Figures 7c–7f). For the ITF, topography at 1°N and 6°N bounds the transport (Figures 7a and 7b), with a small transport bound taken from 0° to 1°N and along the equator, to compensate for the small leakage through this passageway. Transport bounds were also taken at 16.5°N to encompass the meridional extent of NEC, and at 8°N for the MC transport and northern recirculation of the NECC. Taken together, the bounds of transport divide the western Pacific into three boxes (Figures 8a and 9a). For consistency, the same lines of constant latitude and longitude were used as bounds for each upper-layer and lower-layer. However, the locations of currents within these layers may differ. The annual cycle is the mean transport for each calendar month averaged over all years from WPOSE (2009–2017). The interannual variability was assessed by removing the annual cycle.

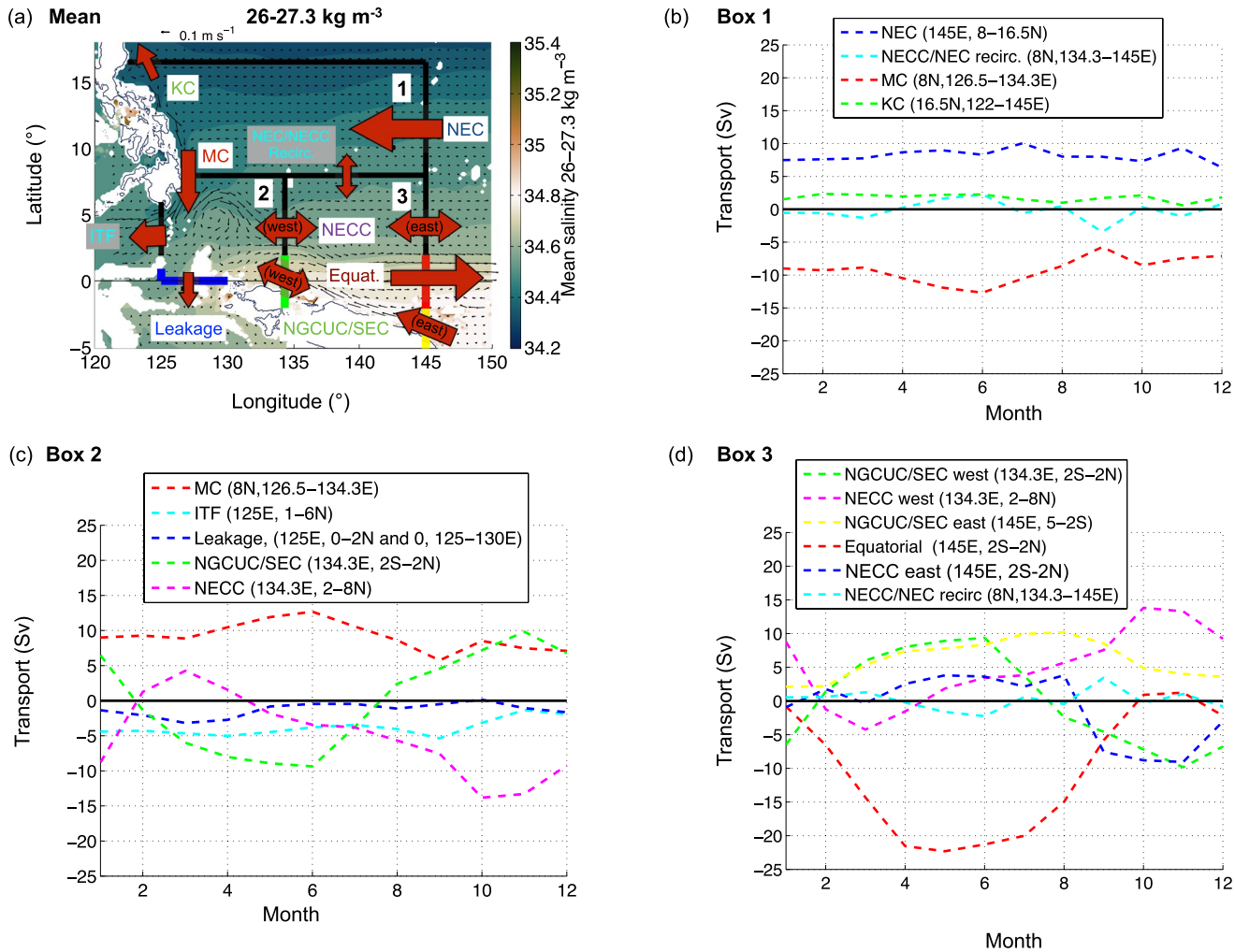

Figure 9. (a) WPOSE mean velocity (arrows) and salinity (color contours) in the lower layer (26–27.3 kg m^{-3}). Boxes (Boxes 1–3) indicate the partitions for annual transport. Arrows label main currents. Lower-layer annual volume transport for (b) Box 1, (c) Box 2, and (d) Box 3. Transport into the box is positive and transport out of the box is negative. Green (yellow) lines along 134.3°E (145°E) indicate the bounds for the NGCUC/SEC west (east) transport. The red line at 145° indicates the bounds of the equatorial transport. Mean transport, and annual and interannual standard deviations of transport for these bounds are given in Figure 10.

5.1. Annual Transport

The annual volume transport variability was calculated for each of the upper (surface-26 kg m^{-3}; Figure 8) and lower (26–27.3 kg m^{-3}; Figure 9) layers. The transport "boxes" encompass the following areas: Box 1 is north of 8°N (122°–145°E, 8°–16.5°N), Box 2 is south of 8°N and west of 134.3°E, encompassing the division of transport from the MC and NGCUC inflow into the ITF and NECC (125°–134.3°E, 0°–8°N), and Box 3 is south of 8°N, and east of 134.3°E, capturing the inflow along the equator, and outflow of the NECC (134.3°–145°E, 5°S–8°N; see Figure 8 for exact integration bounds). For the annual cycle, transport orientation was chosen such that volume transport into the box is positive and transport out of the box is negative. The following sections summarize the annual cycle of the upper (Section 5.1.1; Figure 8) and lower (Section 5.1.2; Figure 9) layers, with a summary of the mean and annual variability (standard deviation) of currents for each of these layers documented in Table 2 and displayed in Figure 10.

5.1.1. Upper Layer

The mean velocity and salinity averaged within the upper layer are shown with the transport bounds in Figure 8a. The salinity extrema decay along the direction of flow, such as that of the NPTW carried by the NEC. There is a

Table 2
Mean Volume Transport, and Annual and Interannual Volume Transport Standard Deviations for Major Currents in the Far Western Pacific From WPOSE

	Layer	Mean transport	Annual standard deviation	Interannual standard deviation
NEC	Upper	−30.9	2.5	4.5
145°E, 8°–16.5°N	Lower	−7.0	1	4.6
KC	Upper	9.5	3.1	3.0
16.5°N, 122°–145°E	Lower	−1.7	0.5	3.1
MC	Upper	−21.2	1.3	4.9
8°N, 126.5°–134.3°E	Lower	−9.2	2.0	5.2
ITF	Upper	−6.1	3.3	3.3
125°E, 1°–6°N	Lower	−3.8	1.2	1.4
LEAKAGE	Upper	−1.6	2.2	2.2
125°E, 0°–1°N and 0°, 125°–130°E	Lower	−1.2	1	1.8
NECC	Upper	27.3	4.8	9.0
134.3°E, 2°–8°N	Lower	5.2	5.8	9.1
NGCUC/NGCC/SEC	Upper	−15.1	5.0	7.7
134.3°E, 2°S–2°N	Lower	−0.1	7.0	7.7
NECC	Upper	20.0	3.7	10.1
145°E, 2°–8°N	Lower	1.2	5.0	8.8
Equatorial	Upper	−2.8	6.3	7.9
145°E, 2°S–2°N	Lower	10.5	9.4	8.4
NGCUC/NGCC/SEC	Upper	−9.8	3.4	2.4
145°E, 5°–2°S	Lower	−6.2	2.9	3.1
NECC/NEC recirc.	Upper	3.5	3.5	3.7
8°N, 134.3°–145°E	Lower	−0.1	1.5	4.4

strong salinity front across the NECC as the relatively fresh North Pacific Tropical Water meets the saline South Pacific Tropical Water brought in from the NGCUC/NGCC/SEC.

In Box 1 (Figure 8b), inward transport is from the NEC and, at times, the northward NECC recirculation. Outflow occurs in the MC and KC. The annual cycle in this box is small, with annual standard deviations on the order of a 1–3 Sv (Table 2, Figure 10). The NECC/NEC recirculation has the greatest transport from January to April, coinciding with build-up of the MD. Concurrently, the NEC and KC transports are at their greatest magnitude. This results in a remarkably steady MC, which maintains roughly 20 Sv of annual volume transport.

In Box 2 (Figure 8c), there is inflow from the equatorward MC and the poleward NGCUC/SEC. Net outflow occurs through the ITF into the Makassar Strait, and the eastward NECC. A southern portion of the ITF that flows into the Maluku Sea is termed "Leakage", as annual transports are small and may reverse. The NGCUC/SEC and seasonal NGCC provide inflow from the southeast, with transport varying from 8 to 23 Sv. There is eastward outflow in the NECC with transport ranging from 20 to 35 Sv. The annual cycle is greatest for the NCGUC/NGCC/SEC and NECC, with annual standard deviations of about 5 Sv (Table 2, Figure 10). The combined ITF and Leakage have a similar magnitude of annual variability, even though their combined mean transport is less than 7 Sv.

In Box 3 (Figure 8d), annual transport is balanced between the NECC (20–35 Sv), equatorial inflow/outflow (0–10 Sv), the NGCUC/NGCC/SEC (8–12 Sv), and northward recirculation in the MD (0–10 Sv). The NGCUC/NGCC/SEC has two components, the net inflow at 145°E, and the net outflow at 134.3°E (Figure 8d). Similarly, the NECC has two components, the net inflow at 134.3°E and the net outflow at 145°E. Annual transport has standard deviations of 3–6 Sv (Table 2, Figure 10). The standard deviation in annual transport is slightly lower at 145°E than at 134.3°E, likely from changes in velocity or westward penetration of flow from the South Pacific

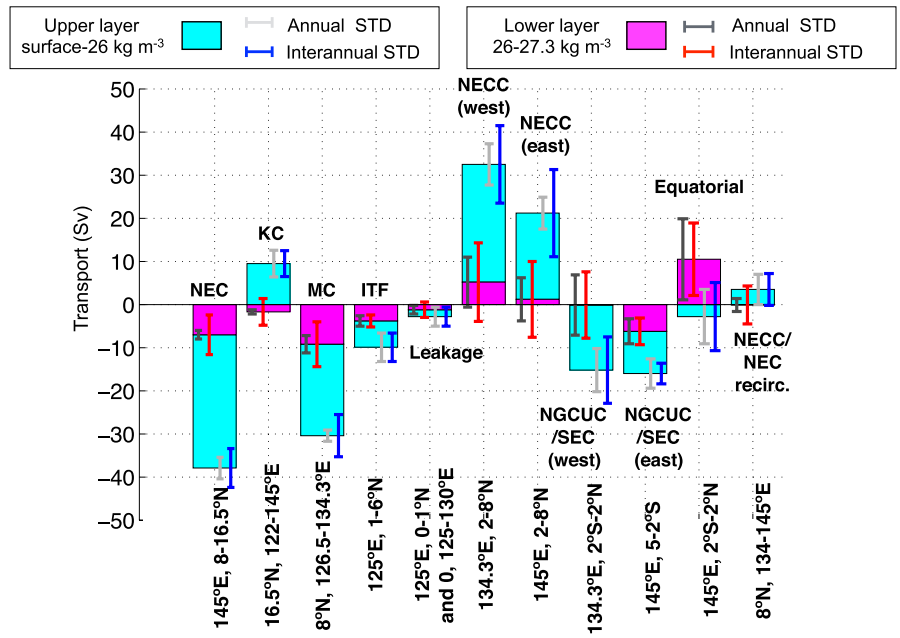

Figure 10. Mean volume transport for the upper (surface-26 kg m^{-3}; cyan) and lower (26–27.3 kg m^{-3}; magenta) layers with annual and interannual standard deviations of transport for each layer. Each bin is labeled by current and range of integration, corresponding to Figures 8a and 9a and Table 2. The NGCUC/SEC (west) and NECC/NEC recirc. have mean lower layer transports near zero. Mean transport is positive (negative) for northward/eastward (southward/westward) transports.

(Figure 6). Annual variability along the equator is also large and net transport reverses (Figure 8d). This may be from a combination of changes in the location and strength of the currents. The equatorial transport limits of 2°S to 2°N are not necessarily natural transport bounds for the upper layer at 145°E (e.g., Figures 6 and 7e).

5.1.2. Lower Layer

Mean velocity and salinity averaged within the lower layer are shown in Figure 9a. As the lower-layer circulation is weaker than that of the upper layer, the scales differ between Figures 8 and 9. In Box 1 (Figure 9b), the annual cycle of lower-layer transport is about half the magnitude or less than that of the upper layer (Figure 8b and Table 2). For the MC, annual transport variability in the lower layer exceeds that of the upper layer.

In Box 2 (Figure 9c), magnitudes of mean transport are half those of the upper layers but with greater variability. The greatest annual variability is from the subthermocline inflow of the NGCUC/SEC and outflow of the NECC along the eastern side of the box (Table 2). Transport from 2° to 8°N changes direction below the NECC, as does the equatorial flow from 2°S to 2°N. (Lower-layer transport from 2° to 8°N is labeled as "NECC" in Figure 9, as the lower layer transport bounds correspond to those of the upper layer, however, it is commonly known as the NSCC, as previously described.) The change in net transport direction from the NGCUC/SEC at 134.3°E is related to its westward penetration (Figures 6e–6h). The transport increase in the fall is in phase with an increase in the upper-layer transport and occurs when the NECC is at its southernmost position (Figures 6c and 6d)

In Box 3 (Figure 9d), annual volume transport variability is large (Table 2). Along the equator (2°S–2°N), the lower-layer mean transport and its annual variability exceed that of the upper-layer, indicative of a strong EUC. The eastward equatorial transport peaks from April to July, before the summertime southern meander and strengthening of the surface NECC (Figure 6c), highlighting the difference in phase of the annual cycle of transport between the upper and lower layers.

5.2. Interannual Transport Variability

The interannual volume transport variability exceeds the annual variability in the region, with a few exceptions (Table 2; Figure 10). From 2009 to 2017, the standard deviation of interannual volume transport for the NEC

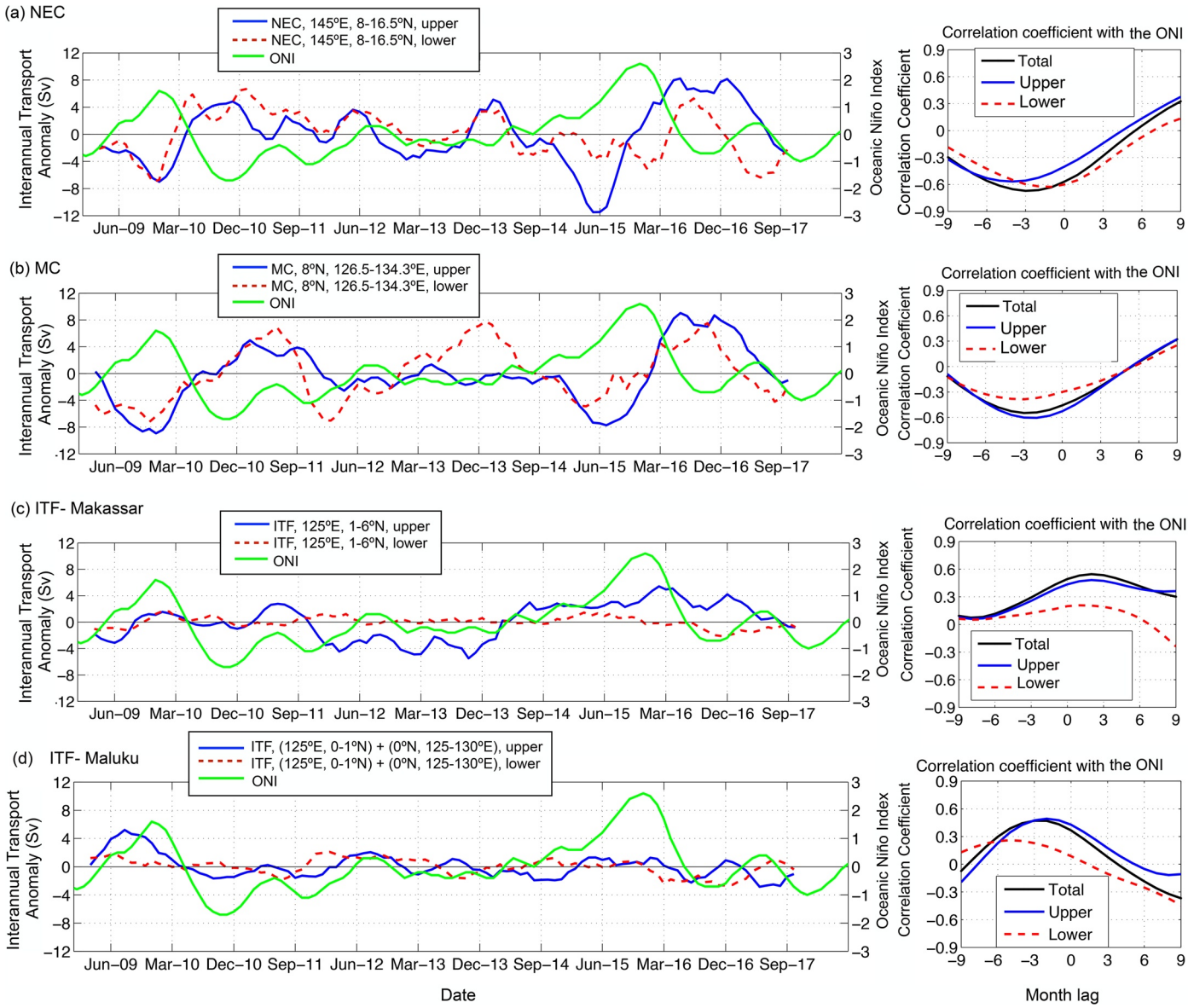

Figure 11. WPOSE upper- (surface-26 kg m^{-3}) and lower- (26–27.3 kg m^{-3}) layer interannual volume transport anomalies (left panels) and their correlation with the ONI (right panels) for transport integrated across (a) the NEC, (b) the MC, (c) the ITF-Makassar (Strait), and (d) Leakage to the ITF. Transport bounds are provided in each legend. Correlation coefficients are shown for the lead/lagged linear regressions of the total transport (surface-27.3 kg m^{-3}), the upper-layer transport, and the lower-layer transport with the Oceanic Niño Index (ONI). Negative (positive) indicates the ONI lags (leads) the transport.

was 15%–25% of the mean transport and for the MC it was 25% of mean transport, roughly double or triple of the annual variability. For the NECC, the standard deviation was 30%–50% of the total mean transport. For the ITF and equatorial flow, annual and interannual transport variabilities were of roughly the same magnitude. Interannual transport variability was likely related to ENSO, the leading cause of interannual variability in the region. Time series of interannual transport anomalies and their correlation with ENSO are shown for the NEC, MC, and ITF/Leakage in Figure 11, and for the NECC, NGCUC/NGCC/SEC, and equatorial regions in Figures 12 (134.3°E) and 13 (145°E), focusing on the currents that displayed the greatest interannual variability. Transport anomalies were smoothed with a 5-month running mean to be more readily compared to the Oceanic Niño Index (ONI). Cross-correlation coefficients with the ONI were calculated for each of the total, upper-layer, and lower-layer transports. Note that there are different vertical scales of transport anomalies used in Figures 11–13.

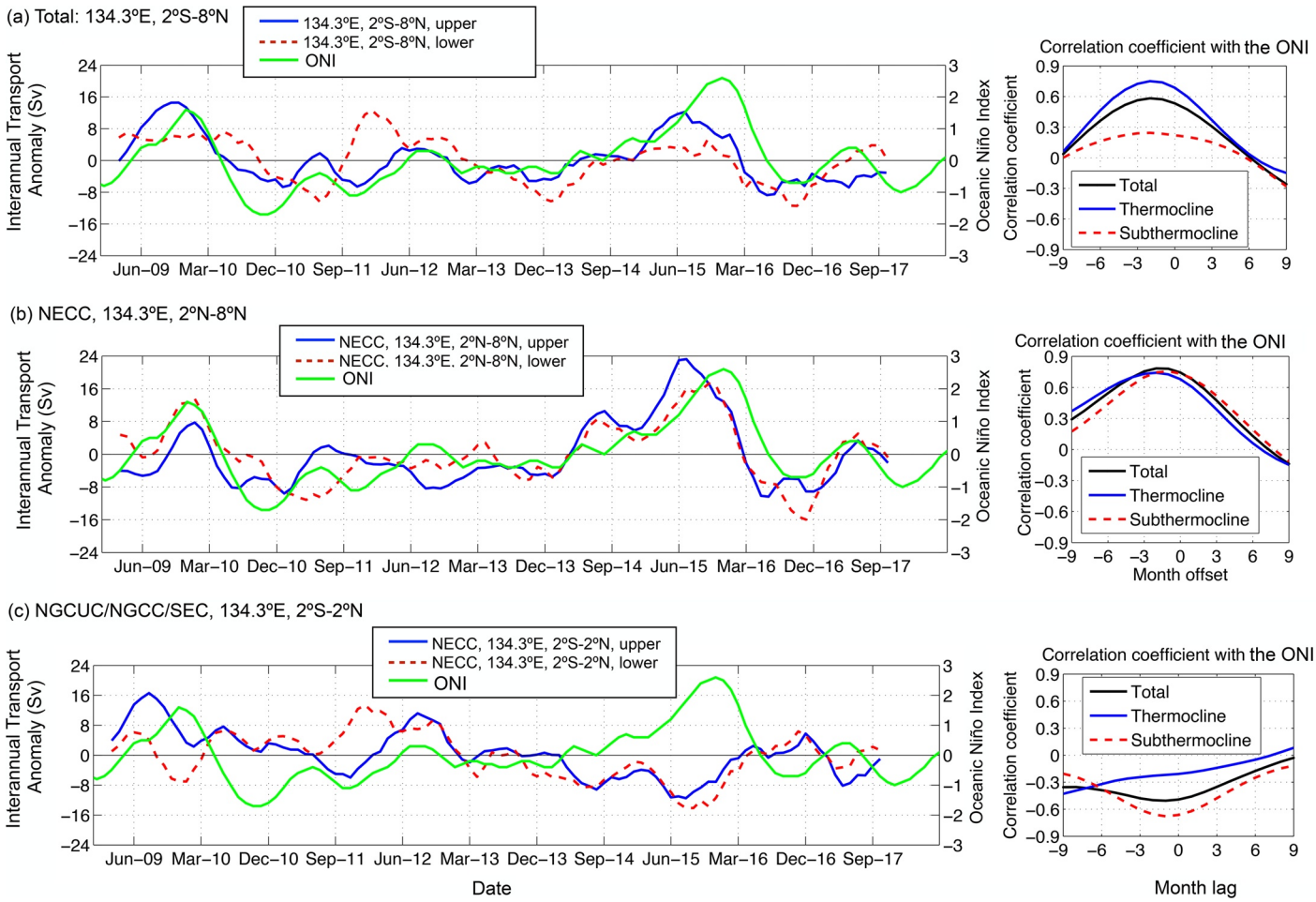

Figure 12. WPOSE upper- (surface-26 kg m^{-3}) and lower- (26–27.3 kg m^{-3}) layer interannual transport anomalies (left) and their correlation with the Oceanic Niño Index (ONI) (right) integrated from (a) 2°S–8°N, (b) 2°–8°N, and (c) 2°–2°N. Correlation coefficients are shown for the lead/lagged linear regressions of the total transport (surface-27.3 kg m^{-3}), the upper-layer transport, and the lower-layer transport with the ONI. Negative (positive) indicates the ONI lags (leads) the transport.

5.2.1. NEC, MC, and ITF/Leakage

The NEC and MC had strong interannual volume transport variability that was associated with ENSO. Transport anomalies were large at the peak of the 2009/10 El Niño, with a transport increase of about 8 Sv for each of the NEC (Figure 11a) and the MC (Figure 11b; Negative transport anomalies indicate an anomalous transport in either the westward or southward direction). These anomalies occurred in each of the upper and lower layers. During the prolonged 2010/11 La Niña, volume transport decreased for each of these currents. In 2015, the greatest NEC upper-layer transport anomaly preceded the peak of the 2015/2016 El Niño, with transport leading the ONI by almost 6 months (Figure 11a). A volume transport anomaly of lesser magnitude occurred a month later in the MC (Figure 11b). During these shifts, lower-layer and upper-layer transport anomalies were not in phase for the NEC, but were in phase for the MC. Following the 2015/16 El Niño, the NEC and MC each had the greatest decrease in transports, even though a La Niña did not develop. The total transports of each of the MC and NEC were correlated with the ONI, leading it by about 3 months even though the peak anomalies did not occur at the same time with respect to the El Niño events.

The relationship of the ITF transport to ENSO was not straightforward. From 2009 to 2011, over the 2009/10 El Niño and 2010/11 La Niña, upper-layer transport anomalies were small (Figure 11c). Then, in 2012 a prolonged increase in upper-layer transport through the Makassar Strait (2012–2014), was followed by an extended decrease (2014–2017). The ITF leakage had a large eastward anomaly in transport during the 2009 El Niño, but in general, anomalies were small and had low correlation with ENSO (Figure 11d). Lower-layer transport anomalies were

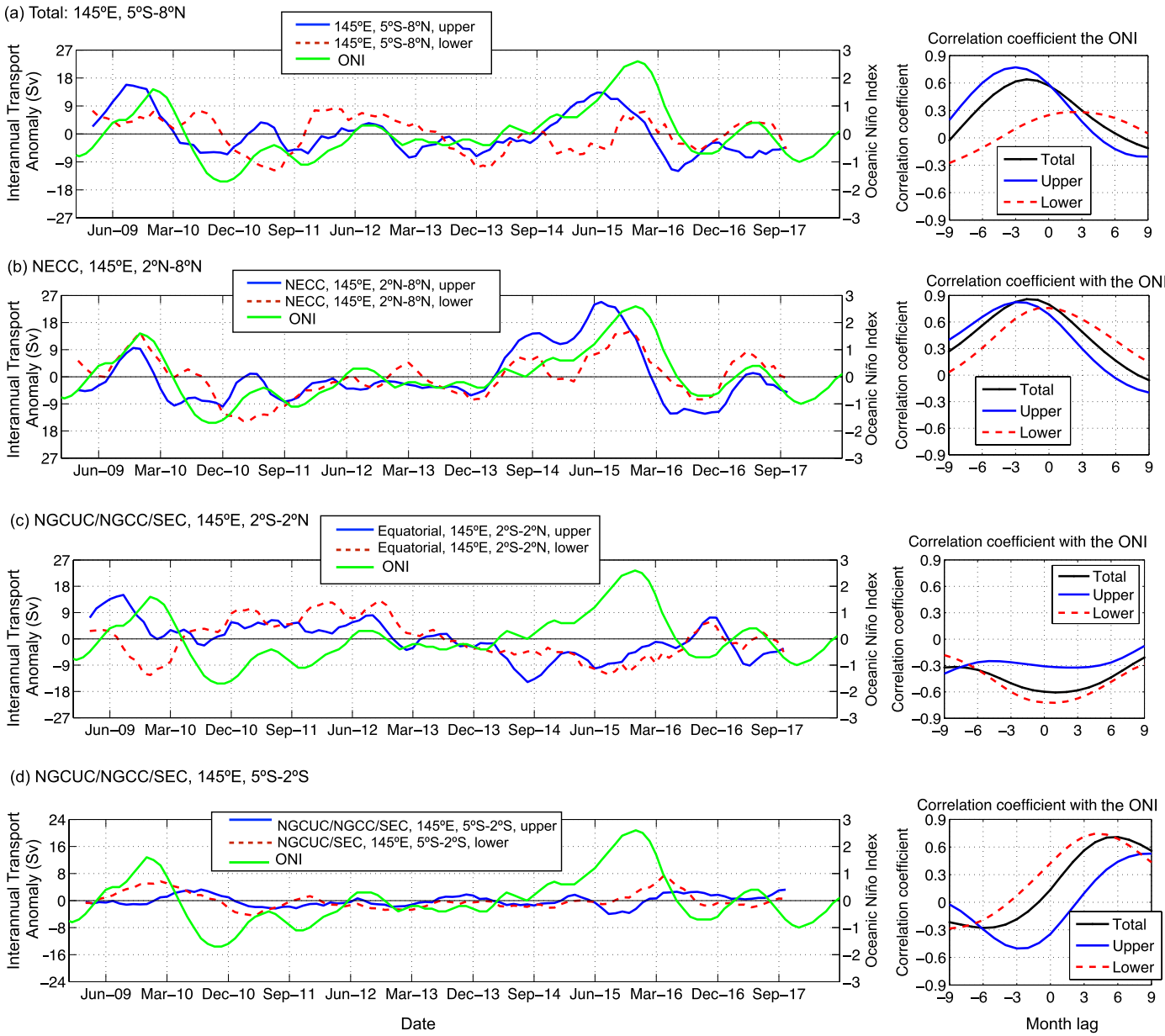

Figure 13. WPOSE upper- (surface-26 kg m^{-3}) and lower- (26–27.3 kg m^{-3}) layer interannual volume transport anomalies (left) and their correlation with the Oceanic Niño Index (ONI) (right) integrated along 145°E from (a) 5°S to 8°N, (b) 2° to 8°N, and (c) 2°S to 2°N, and (d) 5° to 2°S.Correlation coefficients are shown for the lead/lagged linear regressions of the total transport (surface-27.3 kg m^{-3}), the upper-layer transport, and the lower-layer transport with the ONI. Negative (positive) indicates the ONI index lags (leads) the transport.

neutral for the ITF. The upper-layer transport was correlated with the ONI, lagging it by about 3 months, whereas the lower-layer transports showed no correlation.

5.2.2. NECC, NGCUC/NGCC/SEC, and Equatorial

South of 8°N, interannual transport anomalies at 134.3°E (Figure 12) and 145°E (Figure 13) were roughly twice the magnitude of those of the MC and the NEC. Along 134.3°E, the transport anomalies of the NECC (2°–8°N; Figure 12b) were correlated with ENSO. The increase in transport was concurrent with the 2009/10 El Niño and led the 2015/16 El Niño by almost 6 months. The lower-layer transport was phase-matched with that of the upper-

layer. Correlations of each of the upper-layer and lower-layer transports with the ONI were significant, leading the ONI by 2 months. Along the equator (2°S–2°N), interannual anomalies were positive in 2009, likely caused by a southward meander of the NECC (Figure 7c). The opposite scenario occurred before the 2015/16 El Niño; westward transport, in phase with the eastward NECC (Figure 12b), increased in both layers (Figures 7c and 12c).

At 145°E (Figure 13), interannual volume transport anomalies were large compared to mean transports. The upper layer transport anomaly of the NECC peaked at 18 Sv, roughly twice the mean transport (Figure 13b). In the lower layer, transport anomalies were large and synchronous with those of the upper layer. The correlation with the ONI was significant, with upper-layer transport anomalies leading the ONI by 3 months, and the lower-layer anomalies in phase with the ONI.

Along the equator (145°E, 2°S–2°N), volume transport anomalies were affected by the southward meander of the NECC during the 2009/10 El Niño and its contraction northward during the 2015/16 El Niño (Figures 7e and 13c). The upper-layer anomalies switched from being mostly positive from 2009 to 2013 (increased eastward flow), to mostly negative from 2014 to 2017 (reduced eastward flow). The lower-layer anomalies had a greater correlation with the ONI, with decreased eastward flow during El Niño (Figures 7f and 13c). The South Pacific volume transport anomalies (5°–2°S) for each upper and lower layers were small but differed in both phase and direction (Figure 13d). It is ambiguous, given the time series, whether the upper layer led or lagged the ONI, but there tended to be increased westward flow during El Niño, with a reduction immediately following the peak. The lower-layer transport had a significant correlation ($R > 0.7$) with the ONI and lagged by about 4 months, during which time there was a reduction in westward flow.

Summing across all currents at 134.3°E (2°S–8°N; Figures 12a) and 145°E (5°S–8°N; Figure 13a) provides the net interannual transport anomalies across both the NECC and equatorial flow. Most of the anomalous inflow from the NGCUC/NGCC/SEC/Equator was likely compensated by the outflow of the NECC (Figure 7). However, in 2009, there may have been a more complicated balance of the NGCUC/NGCC/SEC, ITF, MC, and NECC. The interannual upper-layer total transport anomaly was well correlated with the ONI, with increased eastward flow leading by 2 months at 134.3°E and 3 months at 145°E. The lower-layer transport anomalies at 134.3° and 145°E were positive (increased eastward flow) during El Niño, but they showed little correlation with the ONI.

6. Discussion

6.1. The 2009/10 and 2015/16 El Niño Events

From 2009 to 2017, interannual transport anomalies wobbled like a top; North and South Pacific transports were not in phase, and to the south of 8°N, the upper-layer and lower-layer were also not in phase. However, there was a clear association between transport and ENSO events, particularly in the anomalous increase of transport through the region before and during the strong 2015/16 El Niño event. The transport increase in the tropical North Pacific circulation cell from late 2014 to 2015 coincided with an increase in westward transport along the equator. The combined transports fed an exceptionally large NECC throughout 2014 and 2015, which preceded the peak of the El Niño in 2016.

Averaging over periods of anomalous transport or ENSO state for each the upper layer (Figure 14) and lower layer (Figure 15) provides a way to examine the differences in isopycnal gradients that drive geostrophic transport and along-equatorial flow. These periods were chosen from January 2009 to February 2010 (Figures 14b and 15b), during the 2009/10 El Niño; March 2010 to March 2012 (Figures 14c and 15c), during extended La Niña-like conditions; April 2012 to March 2014 (Figures 14 and 15d), during ENSO neutral conditions; April 2014 to December 2015 (Figures 14e and 15e), corresponding to transport anomalies before and during the strong 2015/16 El Niño; and January 2016 to December 2017, during the adjustment of El Niño to neutral conditions (Figures 14f and 15f). The mean circulation is, in general, perpendicular to the gradients in the layers, except for in the equatorial region (Figures 14a and 15a).

Before, and during an El Niño, most of the region shoals, characteristic of the first EOF-mode (zonal tilt) of ENSO (Meinen & McPhaden, 2000). However, the magnitudes differed between the El Niño events. Shoaling of the thermocline was weak in the MD region during the 2009/10 El Niño (Figure 14b), and strong preceding and during the 2015/16 El Niño (Figure 14e). The differences in magnitude and phase of the 2009/10 and 2015/16

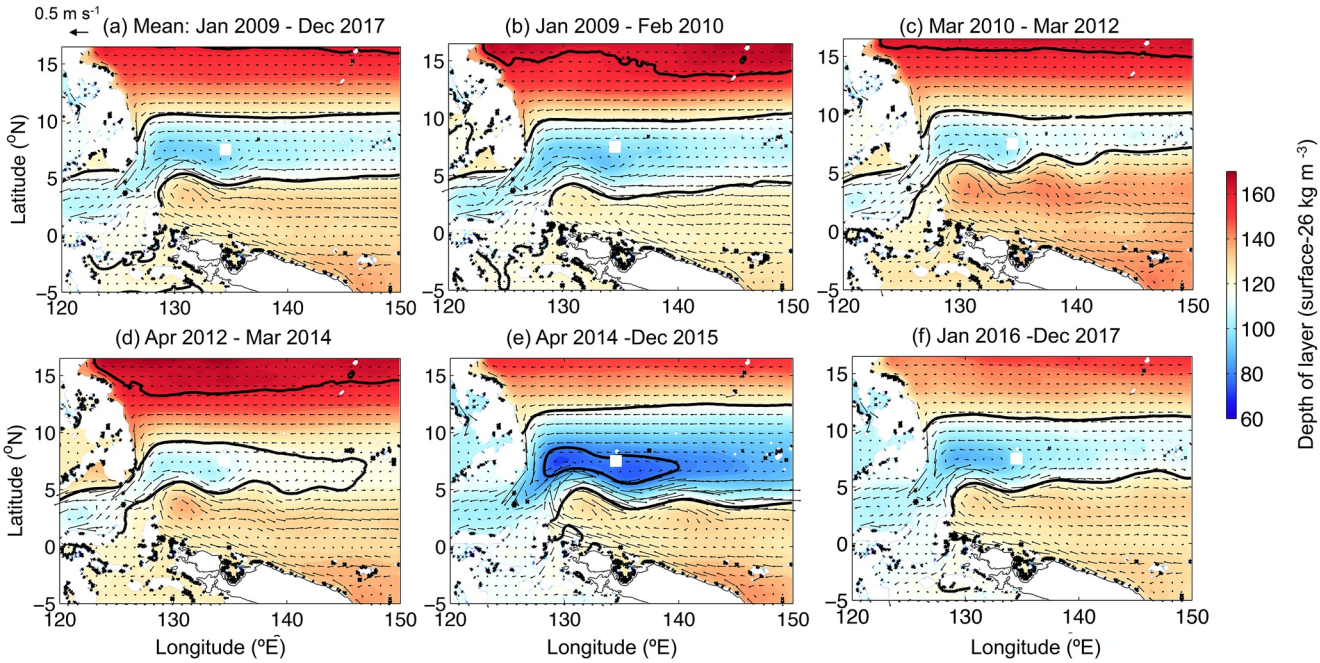

Figure 14. Average of WPOSE velocity and depth of upper layer (surface-27.3 kg m^{-3}) from (a) January 2009 to December 2017, (b) January 2009 to February 2010, (c) March 2010 to March 2012, (d) April 2012 to March 2014, (e) April 2014 to December 2015, and (f) January 2016 to 2017. Thick black lines are contours at 40 m depth intervals.

El Niño events are perhaps unsurprising. There is growing recognition that El Niño events vary in strength and forcing (Capotondi et al., 2020; Santoso et al., 2019). The 2009/10 El Niño has been considered on several metrics to be a Central Pacific (CP) El Niño event, whereas the 2015/16 El Niño was an Eastern Pacific (EP) event (Capotondi et al., 2020).

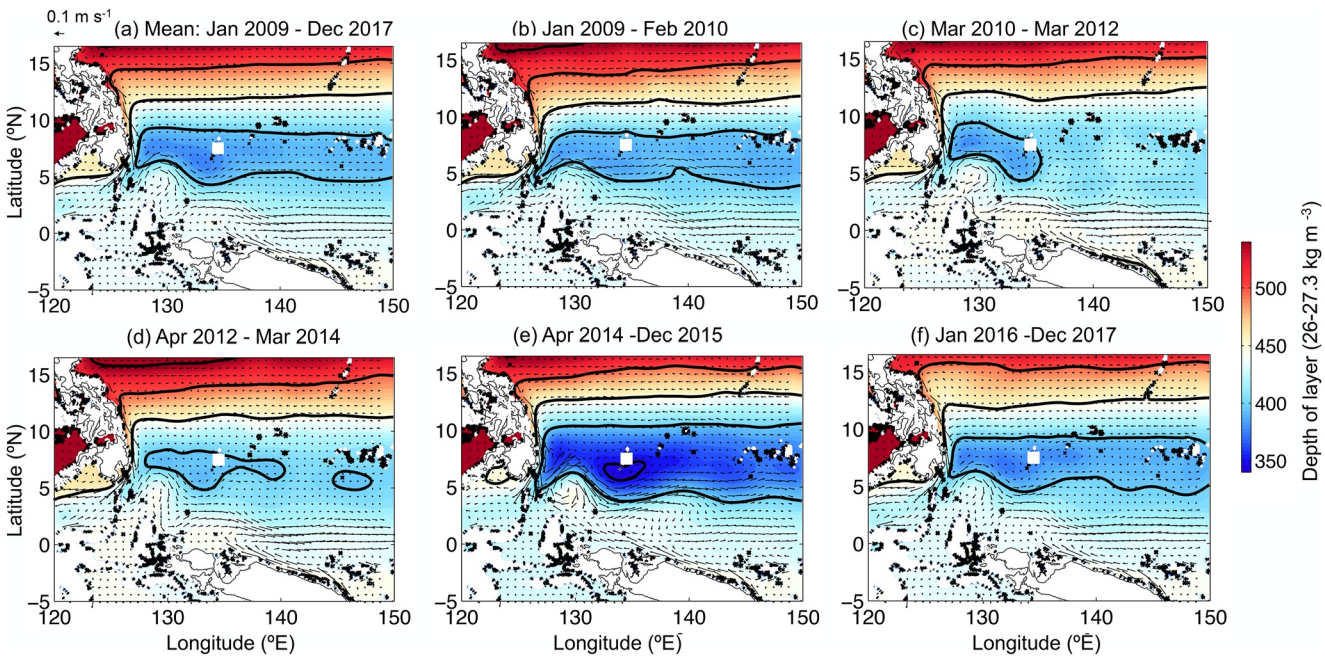

Figure 15. Average of WPOSE velocity and depth of lower layer (26–27.3 kg m^{-3}) from (a) January 2009 to December 2017, (b) January 2009 to February 2010, (c) March 2010 to March 2012, (d) April 2012 to March 2014, (e) April 2014 to December 2015, and (f) January 2016 to 2017. Thick black lines are contours at 50 m depth intervals.

For the 2009/10 El Niño (January 2009 to February 2010; Figure 14b), the region poleward of 10°N deepened, increasing the NEC and MC transports and thus NECC transport. During this period, there was little change in the NGCUC/SEC/Equatorial flow, meaning that the increased NECC transport originated in the North Pacific. The deepening north of 10°N, and shoaling (in comparison to the mean) south of 10°N may indicate more of the meridional tilt mode (second EOF-mode) associated with ENSO.

In contrast, before and during the 2015/16 El Niño, the shoaling in the region of the MD was extreme, creating pressure gradients that increased zonal transport for the NEC, NGCUC/SEC, and NECC, and decreased transport for the ITF. The shoaling followed an extended 2010–2011 La Niña, and even further deepening of the thermocline during 2013 (an ENSO neutral period), consistent with the traditional theory of warm water building up in the western Pacific before El Niño events (Wang & Picaut, 2004; Wyrtki, 1975). In response, the NECC shifted northward where the meridional gradient was strongest. The initial strengthening of the NECC was in phase with the annual cycle, as is typical of strong ENSO events (Clarke, 2014). This type of buildup and subsequent strengthening of the NECC before an El Niño event was observed before the 1982/83, 1994/95, and 1997/98 El Niños, and can play an important role in heat discharge (Lu et al., 2017; Meinen & McPhaden, 2001; Zhang & Clarke, 2017).

The far western Pacific was experiencing El Niño-like conditions (increased transport, shoaling thermocline) throughout 2014 and into 2015. A few transport anomalies began in mid-2014: an anomalous decrease in the ITF (positive anomaly), and anomalous inflow in the equatorial pacific (2°S–2°N) and outflow in the NECC. However, these were largely compensatory. A positive (eastward) interannual transport anomaly began at 145°E in September 2014, coinciding with brief westerly wind-bursts at this longitude (McPhaden, 2015; Schonau, 2017). Anomalous NEC and NECC transports continued into 2015, and westerly wind-bursts reappeared, this time extending further east to 170°–190°E (Hu & Fedorov, 2019). The resurgence of El Niño in 2015 suggests that the NECC transport of warm water may have helped sustain the 2015/16 event, as suggested by McPhaden (2015).

In contrast, the upper layer in the South Pacific did not have dramatic depth changes during the 2015/16 El Niño, remaining at a similar depth as during the previous La Niña and ENSO-neutral period (Figure 14e). Geostrophic current anomalies in the North Pacific tend to lead the ONI, whereas those in the South Pacific lag the ONI (Johnston & Merrifield, 2000; Schonau, 2017). This lead/lag relationship is correlated with the EOF-1 (zonal) mode for the South Pacific, and the EOF-2 (meridional) mode in the North Pacific with strengthening of the NECC and weakening of the SEC prior to the El Niño and the opposite occurring following the mature stage of El Niño (Johnston & Merrifield, 2000; Meinen & McPhaden, 2001). Glider observations confirmed this in 2015/16, with increased equatorward transport in the Solomon Sea slightly lagging the El Niño (Kessler et al., 2019). In the North Pacific, as the El Niño decayed, a rapid readjustment of the thermocline in 2016 caused the NECC transport to decrease dramatically (Schönau et al., 2019). From January 2016 to August 2017 (Figure 14f), interannual transport anomalies reversed in direction (Figures 11a, 11b, 12a, and 13a) and normal conditions resumed.

6.2. The Upper Layer

The annual and interannual dynamics associated with western tropical North Pacific thermocline and current anomalies are commonly linked to changes in wind-stress and north to south progression of the Intertropical Convergence Zone (ITCZ). These create local forcing and annual Rossby waves that arrive from the central Pacific (Kessler, 1990; Masumoto & Yamagata, 1991; Qu et al., 2008; Tozuka et al., 2002; Wang et al., 2000). These linear dynamics have been linked to annual variability in current strength and transport between the NEC and NECC, with strong currents/greater transports in the first half of the year for the NEC, and in second half of the year for the NECC (Hsin & Qiu, 2012a; Qiu & Lukas, 1996; Qu & Lukas, 2003). Similar dynamics are also linked to annual variability in the South Pacific, strengthening the currents and transport in boreal summer (Germineaud et al., 2016; Kessler et al., 2019; Ueki, 2003; Zhang et al., 2020). These impact the ITF transport, greater and deeper in the summer, owing to transport splits of the MC and NGCUC (Gordon et al., 2019; M. Li et al., 2021; X. Li et al., 2021). The upper layer WPOSE transports are in general agreement with the phases and magnitudes of annual transport variability (see above references). There have also been observations of the

increase in the NECC before the 1982/83, 1994/95, and 1997/98 El Niño events (Hsin & Qiu, 2012a; Johnston & Merrifield, 2000; Meinen & McPhaden, 2001).

Linear dynamics have often been used to explain thermocline depth variance in the region using a reduced-gravity 1.5-layer Rossby model that allows for the propagation of Rossby waves from the central Pacific (Kessler, 1990; Kim et al., 2004; Tozuka et al., 2002). This model has been in good agreement with transport anomalies in the South Pacific (Kessler & Cravatte, 2013), and SSH anomalies in the bifurcation region of the NEC near 13°N (Qiu & Chen, 2010). However, it performs poorly on interannual timescales in the North Pacific to the south of 8°N (Qiu et al., 2019; Schönau, 2017; Schönau & Rudnick, 2017). The thermocline depth mismatch was especially large during the 2015/16 El Niño event (Schönau, 2017). The region from 2° to 8°N, and west of 150°E has an enormous amount of eddy kinetic energy (EKE), mostly caused by the barotropic instability from the influx of the NECC (X. Chen et al., 2015; Qiu et al., 2019). In a detailed analysis of energetics, Qiu et al. (2019) found that the nonlinear interaction between inward propagating Rossby waves and the existing NECC can create large amplitude changes in SSH. The strength of the NECC observed by WPOSE in 2014 and 2015 had large amplitudes of barotropic and baroclinic EKE conversion rates in this region, which may explain the exceptionally large mismatch of WPOSE with a linear Rossby model during this period.

6.3. The Lower Layer

The goal in dividing the upper-layer and lower-layer volume transports in this study was to investigate the spatial and temporal differences between the two layers, and their response to interannual variability. Unlike the upper layer, which has a primarily linear response to wind-forcing in most regions, the lower layer is dominated by subthermocline currents and eddies (Aziminuddin et al., 2021; Chiang et al., 2015; Chiang & Qu, 2013; Deutrieux, 2009; Firing et al., 2005; Zhang et al., 2021), that are generated by baroclinic and barotropic instability and nonlinear interactions caused by the breakdown of baroclinic Rossby waves (Qiu et al., 2013; Zhang et al., 2021). There has been evidence that the lower-layer transport also has a relationship with interannual variability, with strong impacts on total volume transports for the ITF and MC (Gordon et al., 2019; Schönau & Rudnick, 2017).

The nonlinear interactions and horizontal resolution of WPOSE may cause it to have difficulties in the lower-layer dynamics; however, WPOSE provides reasonable estimates of lower-layer volume transport and its variability in comparison to ARGO and GO. Although circulation is weaker in the lower-layer, it encompasses greater depth (~300–1,000 m) than that of the upper-layer. The lower-layer transport accounts for up to 15%–40% of the total transport in the North Pacific, and up to 40%–80% of the total transport along the equator and in the South Pacific inflow (Table 2, Figure 10).

The lower-layer transport was mostly in phase with the upper-layer transport on interannual timescales, as well as in the depth shifts during the 2009/10 and 2015/16 El Niño event (Figures 11–15). There was deepening north of 10°N during the 2009/10 El Niño (Figure 15b), deepening of the entire region during La Niña and ENSO neutral periods (Figures 15c and 15d), and extreme shoaling of the MD, from 5° to 10°N, before and during the 2015/16 El Niño (Figure 15e). The EUC was strongest along the equator during La Niña.

However, there were annual and interannual differences between the upper-ayer and lower-layer particularly in the region near the equator between 0°–5°N and 135°–145°E, caused by shifts in the NGCUC/SEC and equatorial current strength and meander, with large shifts particularly during the 2015/16 El Niño event (Figures 6, 9d, 14, and 15). In 2009/10 (Figure 15b), the lower layer had similar velocities and depth as the mean (Figure 15a). However, preceding and during the 2015/16 El Niño (Figure 15e), the equatorial eastward flow split into two branches, one below the NECC and one along the equator (Figure 15e), leading to low equatorial transport during this period (Figure 13c). The change in location and strength of the lower-layer component of the HE is also noticeable. During the 2009/10 El Niño (Figure 15b), the lower-layer velocities was very similar to the mean, whereas preceding and during the 2015/16 El Niño (Figure 15e), the HE was stronger and further north, indicative of greater energy, and likely baroclinic and barotropic instability that plays a large role in the lower-layer dynamics.

7. Conclusions

The circulation in the far western North Pacific has notable interannual volume transport variability that was related to ENSO extremes, increasing during El Niño events and at times before these events. WPOSE provided insight into the magnitude and phase of annual and interannual volume transport anomalies as a system, which is valuable given the influence of the western Pacific circulation in the distribution of tropical waters across the equatorial Pacific and Indo-Pacific region. Annual transport anomalies were, in general, small north of 8°N, and large south of 8°N, where annual changes in the ITF, NGCUC/NGCC/SEC, and NEC/MC transports combined to impact the NECC. Interannual transport anomalies were two to three times greater than annual anomalies for the NEC/MC and exceeded or were equal to annual anomalies for the ITF, NGCUC/NGCC/SEC, and NECC. The greatest interannual transport anomalies occurred before the peak of the 2015/16 El Niño. The transports of the NEC, MC, NGCUC/NGCC/SEC, and the NECC all increased beginning in September 2014, a year earlier than the mature 2015/2016 El Niño event. The transport increase followed 2 years of an exceptionally deep thermocline in the region indicating a buildup of warm water. The persistent eastward transport of warm water by the NECC from 2014 to 2015 may have sustained WWV on the equator and continued to push the equatorial ocean into an El Niño in 2015. The changes in interannual transport depend on the relative displacement of the thermocline which can be highly nonlinear in this region.

Although WPOSE was in good agreement with ARGO and GO for mean velocity, transport, and thermohaline properties across the major currents, the lack of significant subthermocline undercurrents in WPOSE may mean that it did not fully capture the subthermocline dynamics and volume transports owing to its horizontal and vertical resolution. These dynamics are captured by the nonlinear breakdown of wind forced annual Rossby waves (Qiu et al., 2013), but since WPOSE is a regional state estimate, it may fail to capture some of these processes. North of 8°N, the lower-layer transport tended to follow that of the upper-layer flow, but in the equatorial region, the lower-layer flow was more variable and not necessarily in the same location as the upper-layer currents. The choice of 26 kg m^{-3} as the division between upper and lower layers may play a part in this. While 26 kg m^{-3} divides the thermocline and subthermocline in water masses originating in the North Pacific, transport of saline Atlantic water may extend to greater densities (e.g., Figure 4d). State estimates with increased model resolution that incorporate tides and assimilate data in the equatorial region could in the future be used to improve the model representation of subthermocline dynamics and transport.

Data Availability Statement

Glider data are available at spraydata.ucsd.edu (Rudnick, 2020). The WPOSE are available upon request to B. Cornuelle and G. Gopalakrishnan and as the Northwest Pacific State Estimate/Reanalysis (NWPac) at http://www.ecco.ucsd.edu/nwpac.html. The 1/12° global HYCOM/NCODA Ocean Reanalysis was funded by the U.S. Navy and the Modeling and Simulation Coordination Office. Computer time was made available by the DoD High Performance Computing Modernization Program. The output is publicly available at http://hycom.org. The HYCOM/NCODA 1/12° global daily analysis can be obtained from the HYCOM Consortium (http://hycom.org/dataserver/). Roemmich and Gilson Argo Climatology are available at http://sio-argo.ucsd.edu/RG_Climatology.html. The Argo data are collected and made freely available by the International Argo Program and the national programs that contribute to it. (http://www.argo.ucsd.edu, http://argo.jcommops.org). The Argo Program is part of the Global Ocean Observing System (Argo, 2020). Aviso absolute dynamic topography MADT-H (2014), is available from CLS Space Oceanography Division at http://www.aviso.altimetry.fr/. The AVISO SSH maps used to compare to MADT WPOSE were obtained from the SSALTO/Developing Use of Altimetry for Climate Studies (DUACS) altimeter product on a ¼° longitude × ¼° latitude grid, produced and distributed by the Copernicus Marine and Environment Monitoring Service (CMEMS; http://marine.copernicus.eu/). The MITgcm code used in this study is checkpoint 64Y and can be obtained from http://mitgcm.org/. The along-track altimetry data can be obtained from Radar Altimetry Database System (RADS) (http://rads.tudelft.nl/rads/index.shtml). The SST data can be obtained from Remote Sensing Systems Inc (http://www.remss.com/). The NCEP/NCAR-Reanalysis-1 atmospheric forcings can be obtained from http://www.esrl.noaa.gov/psd/data/gridded/data.ncep.reanalysis.html.

Acknowledgments
Glider observations and analysis were funded by the Office of Naval Research (ONR) as part of the Origins of Kuroshio and Mindanao Current (OKMC) project through Grants N00014-10-1-0273 and N00014-11-1-0429, and Flow Encountering Abrupt Topography (FLEAT) project Grant N0014-15-1-2488, and by the National Oceanic and Atmospheric Administration (NOAA) through Grant NA20OAR4320278. Publication was supported by ONR under the Island Arc Turbulent Eddy Regional Exchange (ARCTERX) Grant N00014-21-1-2747. The WPOSE we funded by ONR under the FLEAT (N00014-15-1-2285) and Island Arc Turbulent Eddy Regional Exchange (ARCTERX; N00014-21-1-2726) project grants. B. Qiu received funding from the National Aeronautics and Space Administration (NASA) under Grant 80NSSC21K0552. The authors gratefully acknowledge the ECCO consortium, including MIT, JPL, and the University of Hamburg. The authors thank the Instrument Development Group at Scripps Institution of Oceanography for all facets of the operations of Spray underwater gliders, and Pat and Lori Colin at the Coral Reef Research Foundation for their support in Palau.

References

Argo (2000). Argo float data and metadata from Global Data Assembly Centre (Argo GDAC). SEANOE. http://doi.org/10.17882/42182

Azminuddin, F., Lee, J. H., Jeon, D., Shin, C.-W., Villanoy, C., Lee, S., et al. (2021). Effect of the intensified sub-thermocline eddy on strengthening the Mindanao Undercurrent in 2019. *Journal of Geophysical Research: Oceans*, *127*, e2021JC017883. https://doi.org/10.1029/2021JC017883

Bingham, F. M., & Lukas, R. (1994). The southward intrusion of North Pacific intermediate water along the Mindanao coast. *Journal of Physical Oceanography*, *24*, 141–154. https://doi.org/10.1175/1520-0485(1994)024<0141:tsionp>2.0.co;2

Capotondi, A., Wittenberg, A. T., Kug, J.-S., Takahashi, K., & McPhaden, M. (2020). ENSO diversity. In A. Santoso, W. Cai, & M. McPhaden (Eds.), *El Niño Southern Oscillation in a changing climate* (pp. 65–86). American Geophysical Union. https://doi.org/10.1002/9781119548164.ch4

Chassignet, E. P., Hurlburt, H. E., Smedstad, O. M., Halliwell, G. R., Hogan, P. J., Wallcraft, A. J., et al. (2007). The HYCOM (HYbrid Coordinate Ocean Model) data assimilative system. *Journal of Marine Systems*, *65*, 60–83. https://doi.org/10.1016/j.jmarsys.2005.09.016

Chen, L., Jia, Y., & Liu, Q. (2014). Mesoscale eddies in the Mindanao Dome region. *Journal of Oceanography*, *71*, 133–140. https://doi.org/10.1007/s10872-014-0255-3

Chen, X., Qiu, B., Chen, S., Qi, Y., & Du, Y. (2015). Seasonal eddy kinetic energy modulations along the North Equatorial Countercurrent in the Western Pacific. *Journal of Geophysical Research: Oceans*, *120*, 6351–6362. https://doi.org/10.1002/2015JC011054

Chiang, T.-L., & Qu, T. (2013). Subthermocline eddies in the Western Equatorial Pacific as shown by an eddy-resolving OGCM. *Journal of Physical Oceanography*, *43*, 1241–1253. https://doi.org/10.1175/JPO-D-12-0187.1

Chiang, T.-L., Wu, C.-R., Qu, T., & Hsin, Y.-C. (2015). Activities of 50–80 day subthermocline eddies near the Philippine coast. *Journal of Geophysical Research: Oceans*, *120*, 3606–3623. https://doi.org/10.1002/2013JC009626

Clarke, A. J. (2014). El Niño Physics and El Niño predictability. *Annual Review of Marine Science*, *6*, 79–99. https://doi.org/10.1146/annurev-marine-010213-135026

Davis, R. E., Ohman, M. D., Rudnick, D. L., & Sherman, J. T. (2008). Glider surveillance of physics and biology in the southern California Current System. *Limnology & Oceanography*, *53*, 2151–2168. https://doi.org/10.4319/lo.2008.53.5_part_2.2151

Dutrieux, P. (2009). *Tropical Western Pacific currents and the origin of intraseasonal variability below the thermocline* (Ph.D. thesis) (p. 150). University of Hawaii at Manoa. Pubmed Partial Author stitle stitle Volume Page., Structured.

Fine, R. A., Lukas, R., Bingham, F. M., Warner, M. J., & Gammon, R. H. (1994). The Western equatorial Pacific: A water mass crossroads. *Journal of Geophysical Research*, *99*, 25063–25080. https://doi.org/10.1029/94JC02277

Firing, E., Kashino, Y., & Hacker, P. (2005). Energetic subthermocline currents observed east of Mindanao. *Deep Sea Research Part II: Topical Studies in Oceanography*, *52*, 605–613. https://doi.org/10.1016/j.dsr2.2004.12.007

Germineaud, C., Ganachaud, A., Sprintall, J., Cravatte, S., Eldin, G., Alberty, M. S., & Privat, E. (2016). Pathways and water mass properties of the thermocline and intermediate waters in the Solomon Sea. *Journal of Physical Oceanography*, *46*(10), 3031–3049. https://journals.ametsoc.org/view/journals/phoc/46/10/jpo-d-16-0107.1.xml

Gopalakrishnan, G., Cornuelle, B. D., Hoteit, I., Rudnick, D. L., & Owens, W. B. (2013). State estimates and forecasts of the loop current in the Gulf of Mexico using the MITgcm and its adjoint. *Journal of Geophysical Research: Oceans*, *118*, 3292–3314. https://doi.org/10.1002/jgrc.20239

Gordon, A. L. (1986). Inter-ocean exchange of thermocline water. *Journal of Geophysical Research*, *91*, 5037–5046. https://doi.org/10.1029/JC091iC04p05037

Gordon, A. L., & Fine, R. A. (1996). Pathways of water between the Pacific and Indian oceans in the Indonesian seas. *Nature*. https://doi.org/10.1038/379146a0

Gordon, A. L., Napitu, A., Huber, B. A., Gruenburg, L. K., Pujiana, K., Agustiadi, T., et al. (2019). Makassar strait throughflow seasonal and interannual variability: An overview. *Journal of Geophysical Research: Oceans*, *124*, 3724–3736. https://doi.org/10.1029/2018jc014502

Gouriou, Y., & Toole, J. (1993). Mean circulation of the upper layers of the western equatorial Pacific Ocean. *Journal of Geophysical Research*, *98*(22), 495–520. https://doi.org/10.1029/93jc02513

Heimbach, P., Hill, C., & Giering, R. (2002). Automatic generation of efficient adjoint code for a Parallel Navier-Stokes solver. *Paper presented at the Computational Science—ICCS 2002* (pp. 1019–1028). Springer-Verlag. https://doi.org/10.1007/3-540-46080-2_107

Hsin, Y.-C., & Qiu, B. (2012a). Seasonal fluctuations of the surface North Equatorial Countercurrent (NECC) across the Pacific basin. *Journal of Geophysical Research*, *117*. https://doi.org/10.1029/2011JC007794

Hsin, Y.-C., & Qiu, B. (2012b). The impact of Eastern-Pacific versus Central-Pacific El Niños on the North Equatorial Countercurrent in the Pacific Ocean. *Journal of Geophysical Research*, *117*, C11017. https://doi.org/10.1029/2012JC008362

Hu, D., Wu, L., Cai, W., Gupta, A. S., Ganachaud, A., Qiu, B., et al. (2015). Pacific Western boundary currents and their roles in climate. *Nature*, *522*, 299–308. https://doi.org/10.1038/nature14504

Hu, D. X., Cui, M. C., Qu, T. D., & Li, Y. X. (1991). A subsurface northward current off Mindanao identified by dynamic calculation. *Oceanography of Asian Marginal Seas*, 359–365. https://doi.org/10.1016/s0422-9894(08)70108-9

Hu, S., & Fedorov, A. V. (2019). The extreme El Niño of 2015–2016: The role of westerly and easterly wind bursts, and preconditioning by the failed 2014 event. *Climate Dynamics*, *52*, 7339–7357. https://doi.org/10.1007/s00382-017-3531-2

Johnson, G. C., Sloyan, B. M., Kessler, W. S., & McTaggart, K. E. (2002). Direct measurements of upper ocean currents and water properties across the tropical Pacific during the 1990s. *Progress in Oceanography*, *52*, 31–61. https://doi.org/10.1016/S0079-6611(02)00021-6

Johnston, T. M. S., & Merrifield, M. A. (2000). Interannual geostrophic current anomalies in the near-equatorial western Pacific. *Journal of Physical Oceanography*, *30*(1), 3–14. https://doi.org/10.1175/1520-0485(2000)030<0003:igcait>2.0.co;2

Kalnay, E., Kanamitsu, M., Kistler, R., Collins, W., Deaven, D., Gandin, L., et al. (1996). The NCEP/NCAR 40-year reanalysis project. *Bulletin of the American Meteorological Society*, *77*, 437–471. https://doi.org/10.1175/1520-0477(1996)077<0437:tnyrp>2.0.co;2

Kashino, Y., Ishida, A., & Hosoda, S. (2011). Observed ocean variability in the Mindanao Dome Region. *Journal of Physical Oceanography*, *41*(2), 287–302. https://journals.ametsoc.org/view/journals/phoc/41/2/2010jpo4329.1

Kawabe, M., Kashino, Y., & Kuroda, Y. (2008). Variability and linkages of New Guinea coastal undercurrent and lower equatorial intermediate current. *Journal of Physical Oceanography*, *38*, 1780–1793. https://doi.org/10.1175/2008JPO3916.1

Kessler, W., Hristova, H., & Davis, R. E. (2019). Equatorward western boundary transport from the South Pacific: Glider observations, dynamics and consequences. *Progress in Oceanography*, *174*, 208–225. https://doi.org/10.1016/j.pocean.2019.04.005

Kessler, W. S. (1990). Observations of long Rossby waves in the northern tropical Pacific. *Journal of Geophysical Research*, *95*, 5183–5217. https://doi.org/10.1029/JC095iC04p05183

Kessler, W. S., & Cravatte, S. (2013). ENSO and short-term variability of the South Equatorial Current entering the Coral Sea. *Journal of Physical Oceanography*, *43*, 956–969. https://doi.org/10.1175/JPO-D-12-0113.1

Kim, Y. Y., Qu, T., Jensen, T., Miyama, T., Mitsudera, H., Kang, H.-W., & Ishida, A. (2004). Seasonal and interannual variations of the North Equatorial Current bifurcation in a high-resolution OGCM. *Journal of Geophysical Research*, *109*, C03040. https://doi.org/10.1029/2003JC002013
Kuroda, Y. (2000). Variability of currents off the northern coast of New Guinea. *Journal of Oceanography*, *56*, 103–116.
Lien, R.-C., Ma, B., Lee, C. M., Sanford, T. B., Mensah, V., Centurioni, L. R., et al. (2015). The Kuroshio and Luzon Undercurrent east of Luzon Island. *Oceanography*, *28*(4), 54–63. https://doi.org/10.5670/oceanog.2015.81
Lindstrom, E., Lukas, R., Fine, R., Firing, E., Godfrey, S., Meyers, G., & Tsuchiya, M. (1987). The western equatorial Pacific Ocean circulation study. *Nature*, *330*, 533–537. https://doi.org/10.1038/330533a0
Li, M., Yuan, D., Gordon, A. L., Gruenburg, L. K., Li, X., Li, R., et al. (2021). A strong Sub-Thermocline intrusion of the North Equatorial Subsurface Current into the Makassar Strait in 2016–2017. *Geophysical Research Letters*, *48*, e2021GL092505. https://doi.org/10.1029/2021GL092505
Li, X., Yuan, D., Li, Y., Wang, Z., Wang, J., Hu, X., et al. (2021). Moored observations of currents and water mass properties between talaud and Halmahera Islands at the entrance of the Indonesian Seas. *Journal of Physical Oceanography*, *51*(12), 3557–3572. https://journals.ametsoc.org/view/journals/phoc/51/12/JPO-D-21-0048.1.xml
Lu, Q., Ruan, Z., Wang, D.-P., Chen, D., & Wu, Q. (2017). Zonal transport from the western boundary and its role in warm water volume changes during ENSO. *Journal of Physical Oceanography*, *47*, 211–225. https://doi.org/10.1175/JPO-D-16-0112.1
Marshall, J., Hill, C., Perelman, L., & Adcroft, A. (1997). Hydrostatic, quasi-hydrostatic, and nonhydrostatic ocean modeling. *Journal of Geophysical Research*, *102*, 5733–5752. https://doi.org/10.1029/96JC02776
Masumoto, Y., & Yamagata, T. (1991). Response of the western tropical Pacific to the Asian winter monsoon: The generation of the Mindanao Dome. *Journal of Physical Oceanography*, *21*, 1386–1398. https://doi.org/10.1175/1520-0485(1991)021<1386:rotwtp>2.0.co;2
McClean, J. L., Bader, D. C., Bryan, F. O., Maltrud, M. E., Dennis, J. M., Mirin, A. A., et al. (2011). A prototype two-decade fully-coupled fine-resolution CCSM simulation. *Ocean Modelling*, *39*, 10–30. https://doi.org/10.1016/j.ocemod.2011.02.011
McPhaden, M. J. (2015). Playing hide and seek with El Niño. *Nature Climate Change*, *5*, 791–795. https://doi.org/10.1038/nclimate2775
McPhaden, M. J., Busalacchi, A. J., Cheney, R., Donguy, J.-R., Gage, K. S., Halpern, D., et al. (1998). The tropical ocean-global atmosphere observing system: A decade of progress. *Journal of Geophysical Research*, *103*, 14169–14240. https://doi.org/10.1029/97JC02906
Mean absolute dynamic topography MADT-H. (2014). *CLS space oceanography division with help from Cnes Aviso*. Retrieved from http://www.aviso.altimetry.fr/. Accessed 16 August 2016.
Meinen, C. S., & McPhaden, M. J. (2000). Observations of warm water volume changes in the equatorial Pacific and their relationship to El Niño and La Niña. *Journal of Climate*, *13*(20), 3551–3559. https://doi.org/10.1175/1520-0442(2000)013<3551:OOWWVC>2.0.CO;2,
Meinen, C. S., & McPhaden, M. J. (2001). Interannual variability in warm water volume transports in the equatorial Pacific during 1993–99. *Journal of Physical Oceanography*, *31*, 1324–1345. https://doi.org/10.1175/1520-0485(2001)031<1324:iviwwv>2.0.co;2
Qiu, B., & Chen, S. (2010). Interannual-to-decadal variability in the bifurcation of the North Equatorial Current off the Philippines. *Journal of Physical Oceanography*, *40*, 2525–2538. https://doi.org/10.1175/2010JPO4462.1
Qiu, B., Chen, S., Powell, B. S., Colin, P. L., Rudnick, D. L., Schönau, M. C., et al. (2019). Nonlinear short-term upper ocean circulation variability in the tropical western Pacific. *Oceanography*, *28*(4), 22–31. https://doi.org/10.5670/oceanog.2015.78
Qiu, B., Chen, S., & Sasaki, H. (2013). Generation of the North Equatorial Undercurrent jets by Triad baroclinic Rossby wave interactions. *Journal of Physical Oceanography*, *43*, 2682–2698. https://doi.org/10.1175/JPO-D-13-099.1
Qiu, B., & Lukas, R. (1996). Seasonal and interannual variability of the North Equatorial Current, the Mindanao Current, and the Kuroshio along the Pacific western boundary. *Journal of Geophysical Research*, *101*, 12315–12330. https://doi.org/10.1029/95JC03204
Qiu, B., Rudnick, D., Cerovecki, I., Cornuelle, B., Chen, S., Schonau, M., et al. (2015). The Pacific North Equatorial Current: New insights from the origins of the Kuroshio and Mindanao Currents (OKMC) project. *Oceanography*, 24–33.
Qu, T., Gan, J., Ishida, A., Kashino, Y., Tozuka, T., & Schönau, M. (2008). Semiannual variation in the western tropical Pacific Ocean. *Geophysical Research Letters*, *35*, L16602. https://doi.org/10.1029/2008GL035058
Qu, T., Kagimoto, T., & Yamagata, T. (1997). A subsurface countercurrent along the East Coast of Luzon. *Deep-Sea Research Part I*, *44*, 413–423. https://doi.org/10.1175/1520-0485(2003)033<0005:tbotne>2.0.co;2
Qu, T., & Lukas, R. (2003). The bifurcation of the North Equatorial Current in the Pacific. *Journal of Physical Oceanography*, *33*, 5–18.
Roemmich, D., & Gilson, J. (2009). The 2004–2008 mean and annual cycle of temperature, salinity, and steric height in the global ocean from the Argo Program. *Progress in Oceanography*, *82*, 81–100. https://doi.org/10.1016/j.pocean.2009.03.004
Rudnick, D. (2020). Origins of the Kuroshio and Mindanao Current [Data set]. stl Scripps Institution of Oceanography, Instrument Development Group. https://doi.org/10.21238/S8SPRAY9131
Rudnick, D. L., Owens, W. B., Johnston, T. M. S., Karnauskas, K. B., Jakoboski, J., & Todd, R. E. (2021). The equatorial current system west of the Galapagos Islands during the 2014-16 El Nino as observed by underwater gliders. *Journal of Physical Oceanography*, *51*(1), 3–17. https://doi.org/10.1175/jpo-d-20-0064.1
Santoso, A., Hendon, H., Watkins, A., Power, S., Dommenget, D., England, M. H., et al. (2019). Dynamics and predictability of El Niño–Southern Oscillation: An Australian perspective on progress and challenges. *Bulletin of the American Meteorological Society*, *100*, 403–420. https://doi.org/10.1002/2017rg000560
Santoso, A., McPhaden, M. J., & Cai, W. (2017). The defining characteristics of ENSO extremes and the strong 2015/2016 El Niño. *Reviews of Geophysics*, *55*, 1079–1129. https://doi.org/10.1175/2011JCLI4169.1
Schneider, N. (1998). The Indonesian throughflow and the global climate system. *Journal of Climate*, *11*, 676–689. https://doi.org/10.1175/1520-0442(1998)011%3C0676:TITATG%3E2.0.CO;2
Schönau, M. C. (2017). *Transport and thermohaline structure in the western tropical North Pacific*. UC San Diego.
Schönau, M. C., & Rudnick, D. L. (2015). Glider observations of the North Equatorial Current in the western tropical Pacific. *Journal of Geophysical Research: Oceans*, *120*, 3586–3605. https://doi.org/10.1002/2014JC010595
Schönau, M. C., & Rudnick, D. L. (2017). Mindanao current and undercurrent: Thermohaline structure and transport from repeat glider observations. *Journal of Physical Oceanography*, *47*, 2055–2075. https://doi.org/10.1175/jpo-d-16-0274.1
Schönau, M. C., Rudnick, D., Cerovecki, I., Gopalakrishnan, G., Cornuelle, B., McClean, J., & Qiu, B. (2015). The Mindanao Current: Mean structure and connectivity. *Oceanography*, *28*, 34–45. https://doi.org/10.1175/1520-0442(1998)011<0676:titatg>2.0.co;2
Schönau, M. C., Wijesekera, H. W., Teague, W. J., Colin, P. L., Gopalakrishnan, G., Rudnick, D. L., et al. (2019). The end of an El Niño: A view from Palau. *Oceanography*, *32*(4), 32–45. https://doi.org/10.5670/oceanog.2019.409
Schramek, T. A., Cornuelle, B. D., Gopalakrishnan, G., Colin, P. L., Rowley, S. J., Merrifield, M. A., et al. (2019). Tropical western Pacific thermal structure and its relationship to ocean surface variables: A numerical state estimate and forereef temperature records. *Oceanography*, *32*(4), 156–163. https://doi.org/10.5670/oceanog.2019.421
Stammer, D., Wunsch, C., Giering, R., Eckert, C., Heimbach, P., Marotzke, J., et al. (2002). Global ocean circulation during 1992–1997, estimated from ocean observations and a general circulation model. *Journal of Geophysical Research*, *107*. https://doi.org/10.1029/2001JC000888

Talley, L. D. (1993). Distribution and formation of North Pacific intermediate water. *Journal of Physical Oceanography*, *23*, 517–537.

Todd, R. E., Rudnick, D. L., Mazloff, M. R., Davis, R. E., & Cornuelle, B. D. (2011). Poleward flows in the southern California Current System: Glider observations and numerical simulation. *Journal of Geophysical Research*, *116*, C02026. https://doi.org/10.1175/1520-0485(1993)023<0517:dafonp>2.0.co;2

Toole, J. M., Zou, E., & Millard, R. C. (1988). On the circulation of the upper waters in the western equatorial Pacific Ocean. *Deep-Sea Research Part I: Oceanographic Research Papers*, *35*, 1451–1482. https://doi.org/10.1016/0198-0149(88)90097-0

Tozuka, T., Kagimoto, T., & Masumoto, Y. (2002). Simulated multiscale variations in the western tropical Pacific: The Mindanao Dome revisited. *Journal of Physical Oceanography*, *32*, 1338–1359. https://doi.org/10.1175/1520-0485(2002)032<1338:SMVITW>2.0.CO;2

Tsuchiya, M. (1968). Upper waters of the intertropical Pacific Ocean. *Johns Hopkins Oceanographic Studies*, *4*, 50.

Tsuchiya, M., Lukas, R., Fine, R. A., Firing, E., & Lindstrom, E. (1989). Source waters of the Pacific Equatorial Undercurrent. *Progress in Oceanography*, *23*, 101–147. https://doi.org/10.1016/0079-6611(89)90012-8

Ueki, I., Kashino, Y., & Kuroda, Y. (2003). Observation of current variations off the New Guinea coast including the 1997–1998 El Niño period and their relationship with Sverdrup transport. *Journal of Geophysical Research*, *108*, 3243. https://doi.org/10.1029/2002JC001611

Wang, B., Wu, R., & Lukas, R. (2000). Annual adjustment of the thermocline in the tropical Pacific Ocean. *Journal of Climate*, *13*(3), 596–616. Retrieved from https://journals.ametsoc.org/view/journals/clim/13/3/1520-0442_2000_013_0596_aaotti_2.0.co_2.xml

Wang, C., Picaut, J., & au, R. (2004). *Understanding ENSO physics—A review* (pp. 21–48). American Geophysical Union. https://doi.org/10.1175/1520-0442(2000)013<0596:aaotti>2.0.co;2

Wyrtki, K. (1961). *Scientific Results of Marine Investigations of the South China Sea and the Gulf of Thailand 1959–1961* (NAGA Report) (Vol. 2).

Wyrtki, K. (1975). El Niño—The dynamic response of the equatorial Pacific Ocean to atmospheric forcing. *Journal of Physical Oceanography*, *5*, 572–584. https://doi.org/10.1175/1520-0485(1975)005%3C0572:ENTDRO%3E2.0.CO;2

Zhang, L., Hui, Y., Qu, T., & Hu, D. (2021). Seasonal variability of subthermocline eddy kinetic energy East of the Philippines. *Journal of Physical Oceanography*, *51*(3), 685–699. Retrieved from https://journals.ametsoc.org/view/journals/phoc/51/3/JPO-D-20-0101.1.xml

Zhang, X., & Clarke, A. J. (2017). On the dynamical relationship between Equatorial Pacific surface currents, zonally averaged equatorial sea level, and El Niño prediction. *Journal of Physical Oceanography*, *47*(2), 323–337. Retrieved from https://journals.ametsoc.org/view/journals/phoc/47/2/jpo-d-16-0193.1.xml

Zhang, L., Wu, J., Wang, F., Hu, S., Wang, Q., Jia, F., et al. (2020). Seasonal and interannual variability of the currents off the new Guinea coast from mooring measurements. *Journal of Geophysical Research: Oceans*, *125*, e2020JC016242. https://doi.org/10.1175/1520-0485(1975)005<0572:entdro>2.0.co;2